AIAA JOURNAL

Turbulence Modeling in Hypersonic Turbulent Boundary Layers Subject to Convex Wall Curvature

Christian J. Lagares-Nieves,[*] Jean Santiago,[†] and Guillermo Araya[‡]
University of Puerto Rico, Mayaguez, Puerto Rico 00681

https://doi.org/10.2514/1.J060247

Hypersonic boundary layers are crucial in aerospace applications such as hypersonic glide vehicles, rockets, and other advanced space vehicles. Hypersonic flows present unique transport phenomena, including nonnegligible flow compression/dilation, extra strain rates, and large momentum/thermal gradients. In this paper, the performance of three widely used turbulence models is compared, namely, the standard $k-\omega$, the shear stress transport (SST) $k-\omega$, and the Spalart–Allmaras (SA). Based on our turbulence modeling assessment plus the analysis of turbulent transport equation budgets over the experimental geometry from a previous study at a Mach number of 4.9, a moderate supremacy of SA over two equation models was found. To back our conclusions, previous experiments and direct numerical simulations at Mach numbers around 5 have been employed. Overall, the three considered models exhibited a consistent ability to predict first-order statistics both inside and outside the boundary layer. The SST variants were capable of describing the amplification of the constant shear layer induced by the presence of an adverse pressure gradient (APG). Furthermore, the SST $k-\omega$ model also replicated the second peak of turbulence production induced by the concave wall. There was a more aggressive distortion of the boundary layer by APG than by favorable pressure gradient (FPG) as compared with a zero pressure gradient (ZPG) boundary layer. A reasonable performance by Walz's equation in the FPG region is also shown, whereas a notable lack of agreement is seen in the APG. Overall, one could argue for the SA model's best compromise between accurate predictions, numerical stability, and mesh resolution insensitivity in the FPG and ZPG regions, particularly, in outer or integral boundary-layer parameters such as δ or $Re_{\delta 2}$. That being said, the two-equation models are far superior in terms of predicting near-wall parameters (such as u_τ or $u'v'$) or their ability to accurately describe the physics of the hypersonic boundary layer for APG regions (for instance, outer-secondary peaks of turbulent kinetic energy production).

Nomenclature

k = turbulent kinetic energy, $\mathrm{m}^2/\mathrm{s}^2$
Ma = Mach number
P = pressure, Pa
Pr = Prandtl number
Re = Reynolds number
St = Stanton number
T = temperature, K
U = streamwise mean-flow velocity, m/s
u_τ = friction velocity, m/s
V = mean-flow velocity orthogonal to U, m/s
δ = boundary-layer thickness, m
δ_2 = boundary-layer momentum thickness, m
δ^* = boundary-layer displacement thickness, m
θ = dimensionless temperature
μ = dynamic viscosity, Pa·s
ν = kinematic viscosity, m^2/s
ρ = density, kg/m^3
τ = shear stress, Pa
ω = specific dissipation rate, 1/s

Subscripts

comp = compressible flow parameter
inc = incompressible flow parameter
n = wall-normal coordinate
s = wall-parallel coordinate
w = wall parameter
z = spanwise coordinate
∞ or e = freestream or edge conditions

Superscripts

$+$ = inner scaled units
$-$ = time-averaged values
$\sim$ = mass-averaged values

I. Introduction

HIGH-SPEED boundary layers play a vital role in aerospace applications, such as unmanned supersonic/hypersonic vehicles, rockets, scramjets/ramjets, and advanced space vehicles. The development of an extremely thin boundary layer plus the abrupt changes of the wall to freestream flow parameters result in high momentum/thermal gradients with significant impact to the transport phenomena. In this study, three turbulence models are contrasted (the standard: $k-\omega$ [1], the Shear Stress Transport (SST) $k-\omega$ [2], and the Spalart-Allmaras (SA) [3]) in the experimental convex surface geometry of Tichenor et al. [4] at a Mach number of 4.9. In addition, experiments by [5] and DNS by [6–8] are considered to endorse our conclusions. According to Candler [9], hypersonic flows are highly energetic with regions of high temperature, causing internal energy excitation and aerothermodynamics problems [10–12]. Therefore, the obtained understanding of the physics behind hypersonic boundary layers can lead to the development of more efficient control techniques for aerodynamic heating design [13]. Furthermore, Bertin and Cummings [14] performed a review of recent experimental and numerical research efforts done on hypersonic flow and stated that

---

Received 10 October 2020; revision received 25 April 2021; accepted for publication 27 May 2021; published online 20 August 2021.

[*] Ph.D. Research Assistant and Doctoral Candidate, High Performance Computing and Visualization Laboratory, Department of Mechanical Engineering. Student Member AIAA.

[†] Undergraduate Research Assistant, High Performance Computing and Visualization Laboratory, Department of Mechanical Engineering.

[‡] Associate Professor, High Performance Computing and Visualization Laboratory, Department of Mechanical Engineering; araya@mailaps.org. Associate Fellow AIAA.

"there were still many challenges to analyzing and designing high-speed vehicles."

The common denominator of high-speed vehicles is undoubtedly related to the complex geometries, involving concave and convex surface curvatures. An accurate understanding of the governing hypersonic, boundary-layer physics subject to strong curvatures requires simplified geometries to isolate relevant effects. Furthermore, wall temperature effects should also be constrained if the purpose of the study is to understand the impact of curvatures. That being said, the availability of hypersonic wind tunnels is rather scarce, and the achievable near-wall resolution for measurements is highly limited. Furthermore, experimental measurement of the local density or static temperature inside high-speed boundary layers is extremely challenging, or even beyond the bounds of possibility, for contemporary capabilities of experimental devices. On the other hand, numerical simulations of hypersonic, spatially developing, turbulent boundary layers (SDTBL) present unique computational challenges due to the required resolution requirements to solve the smallest scales of motion in direct numerical simulation (DNS). A compromise can be made with large-eddy simulation (LES) that resolves the largest eddies and introduces subgrid models; however, the computational cost of LES can still be prohibitively large at high Reynolds numbers. Hence, Reynolds-averaged Navier–Stokes (RANS) simulations are often employed as an alternative at high Reynolds numbers in order to gain preliminary flow insight. RANS models turbulence with the use of closure models for Reynolds stresses. The accuracy of RANS simulations is highly dependent on the turbulence model chosen as well as its ability to capture important phenomena such as reverse transition or relaminarization, flow separation, and shock/expansion waves. In the past, studies focused on the performance of turbulence models, with varying wall-effects have been conducted such as the comparison of Spalart–Allmaras (SA), the baseline $k-\omega$, and the shear stress transport (SST) $k-\omega$ over a cold, flat plate [15]. They showed that these models were capable of providing good estimates for the skin friction, heat flux at the wall, and velocity/temperature profiles. The models also demonstrated reasonable performance for Reynolds shear stresses, but failed to accurately predict the Reynolds normal stresses and the turbulent transverse heat flux. Currao et al. [16] investigated experimentally and numerically the hypersonic transitional shock-wave–boundary-layer interaction at Mach 5.8. It was stated that Görtler instability was responsible for transition in the separated region. They obtained a value for the curvature parameter (δ/r) of 0.045, according to the RANS solution with the SST $k-\omega$ model. Another relevant study was conducted by Paciorri et al. [17], where the validity of the SA model was evaluated for different configurations (flow over a flat plate, a hollow-cylinder, and over a hyperboloid flare) placed in a hypersonic flow. The main conclusion drawn from their work is the excellent performance of SA for attached flows. This distinction is worth noting as they demonstrate degradation in the model's accuracy for more complex geometries with flow separation. In particular, the SA model underpredicted the size of the separation bubble. Separation in high-speed, compressible flows can be seen in strong concave sections as was alluded in [18–20]. Rivera and Araya [21] evaluated the performance of the standard $k-\omega$ [1] and the SST $k-\omega$ [22] turbulence models on SDTBL under the influence of strong streamline concave curvature at Mach 2.86, whose geometry was reproduced from the experimental setup as in the work of Donovan et al. [23]. Both models performed similarly, and good agreement with experimental wall static pressure was found; however, the $k-\omega$ and SST models significantly overpredicted the skin friction coefficient over the concave wall (∼20%). Funderburk and Narayanaswamy [24] also investigated the effects of curvature on supersonic flow. More precisely, the shock–boundary-layer interactions (SBLIs) caused by a concave wall were analyzed by means of wind tunnel experiments and numerical RANS predictions via the SA turbulence model. Based on wall measurements, they concluded that concave (negative) curvature substantially increased the flow separation zone as compared with the corresponding planar interactions.

On the other hand, the presence of a convex wall curvature in hypersonic flow induces favorable pressure gradient (FPG) and, consequently, flow acceleration and expansion waves. Nicholson et al. [7] performed DNS of turbulent boundary layers subject to weak/strong FPG at a Mach number of 5. Also, they examined several RANS models (Baldwin–Lomax, SA, Wilcox $k-\omega$, and SST $k-\omega$), concluding that all turbulence models predicted reasonably well Reynolds shear stress under a weak FPG, but none of them were able to properly capture the reduction in the Reynolds stresses in strong FPG. López et al. [25] found that the SST $k-\omega$ model exhibited the best performance for supersonic flow conditions when compared with experimental results [25]. They also found that the one-equation model proposed by SA exhibited poor agreement with experimental baselines even when SA is typically advised for external flow in aerodynamic applications [25].

Tichenor et al. [4] conducted experiments to assess the impact of a strong FPG at Mach 4.9 and at high-Reynolds-number ($Re_\theta \approx$ 74,000) conditions. They compared their results to a widely studied zero pressure gradient (ZPG) region and concluded that the strong FPG stabilized the incoming boundary layer, which was noticed by the drastic reduction of the Reynolds stresses and turbulence production. Furthermore, they also pointed out a preferential effect on turbulent structures proportional to the wall distance. Tichenor et al. [4] argued that traditional one- and two-equation models would have a poor performance in the strong pressure gradient (favorable) (SPG) region due to the Boussinesq approximation or eddy viscosity modeling employed in many of these. They assessed the ability of the Launder, Reece, and Rodi SST model [26] to capture Reynolds shear stress trends. They concluded that the recalibrated model was capable of capturing the Reynolds shear stresses naturally.

The present study seeks to address the question posed by Tichenor et al. [4] regarding turbulence model performance on strong pressure gradients. We assess the performance of the standard $k-\omega$ [1], SST $k-\omega$ [2], and SA [3] turbulence models without any recalibration to assess real-world performance with default constants on a two-dimensional computational domain following the description given by Tichenor et al. [4]. The paper is outlined as follows: Sec. II provides some numerical details including solver, inflow condition assessment, and a grid independence study; Sec. III contains results obtained from the numerical solution and a discussion; finally, we provide some major takeaways and conclusions in Sec. IV.

II. Numerical Details

A. Flow Solver, Governing Equations, and Boundary Conditions

1. *Flow Solver and Governing Equations*

General details on the flow solver, spatial discretization scheme, and general constants are given in Table 1. The present work leveraged the density-based solver provided by Ansys Fluent [27] that solves a coupled system of equations. The flux vector is computed through the Advection Upstream Splitting Method (AUSM) flux-vector splitting scheme [29,30]. We selected the AUSM scheme for computing the flux vector due to its ability to provide exact resolution of discontinuities and resistance to oscillations at stationary (and moving) shocks. Furthermore, the implementation provided by Ansys Fluent (i.e., AUSM+) avoids an explicit artificial dissipation and has uniform accuracy and convergence rate for a wide range of Mach numbers [30]. For the finite volume method, we employ the

Table 1 High-level details on the flow solver configuration and assumed fluid properties

Flow solver parameters and fluid properties	Value
Solver formulation	Density based [27]
Discretization scheme	Third-order MUSCL [28]
Specific heat (c_p)	1006.43 J/(kg·K)
Specific heat ratio (γ)	1.4
Sutherland law's reference viscosity	1.716e-5 kg/(m·s)
Sutherland law's reference temperature	273.11 K
Sutherland law's effective temperature	110.56 K
Molecular weight	28.966 kg/kmol
Molecular Prandtl number	0.7
Turbulent Prandtl number	0.85

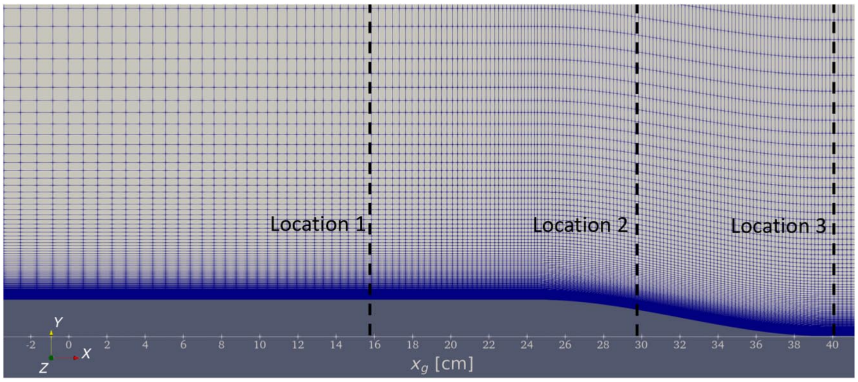

Fig. 1 Reference domain with location labels as in [4]. Flow from left to right.

Monotonic Upstream-centered Scheme for Conservation Laws [28] (MUSCL) due to its second-order spatial accuracy and its applicability on strong shock waves and mathematical discontinuities [31]. When dealing with compression or expansion waves, appropriate considerations must be made with regard to the discretization of the advection terms with jumps in the velocity field. Furthermore, we consider three turbulence models: standard $k-\omega$ [1], SST $k-\omega$ [2], and SA [3]. These models are all based on a notion of a turbulent eddy viscosity (i.e., the Boussinesq hypothesis) as a means to provide closure to the RANS equations (or in the case of compressible flow, Favre-averaged Navier–Stokes equations).

$$\frac{\partial \bar{\rho}}{\partial t} + \frac{\partial}{\partial x_i}(\bar{\rho}\tilde{u}_i) = 0 \tag{1}$$

$$\frac{\partial}{\partial t}(\bar{\rho}\tilde{u}_i) + \frac{\partial}{\partial x_j}(\bar{\rho}\tilde{u}_j\tilde{u}_i) = -\frac{\partial \bar{p}}{\partial x_i} + \frac{\partial}{\partial x_j}(\tilde{\sigma}_{ij} - \overline{\rho u_j' u_i'}) \tag{2}$$

$$\frac{\partial}{\partial t}(\bar{\rho}\tilde{E}) + \frac{\partial}{\partial x_j}\left(\bar{\rho}\tilde{u}_j(\tilde{E}+\bar{p})\right) = \frac{\partial}{\partial x_j}\left(\tilde{u}_i\left(\tilde{\sigma}_{ij} - \overline{\rho u_j' u_i'}\right)\right) - \frac{\partial}{\partial x_j}\tilde{q}_j + \frac{\partial}{\partial x_j}\left(-c_p\overline{\rho u_j' T'} + \overline{u_i'\sigma_{ij}} - \overline{\rho u_j' \frac{(u_i')^2}{2}}\right) \tag{3}$$

The SA model [3] introduces the following equation:

$$\underbrace{\frac{\partial(\bar{\rho}\,\tilde{\nu})}{\partial t}}_{\text{transient term}} + \underbrace{\frac{\partial(\bar{\rho}\,\tilde{\nu}\,\tilde{u}_j)}{\partial x_j}}_{\text{convective term}} = \underbrace{C_{b1}\bar{\rho}[1-f_{t2}]\tilde{S}\,\tilde{\nu}}_{\text{production term}} - \underbrace{\left[C_{w1}f_w - \frac{C_{b1}}{\kappa^2}f_{t2}\right]\bar{\rho}\left(\frac{\tilde{\nu}}{d}\right)^2}_{\text{dissipation term}} + \underbrace{\frac{1}{\sigma}\left[\frac{\partial}{\partial x_j}\left((\mu+\bar{\rho}\,\tilde{\nu})\frac{\partial\tilde{\nu}}{\partial x_j}\right) + C_{b2}\bar{\rho}\left(\frac{\partial\tilde{\nu}}{\partial x_j}\right)^2\right]}_{\text{diffusion term}} \tag{4}$$

The turbulent eddy viscosity is defined as $\mu_t = \bar{\rho}\,\tilde{\nu}\,f_{v1}$, where f_{v1} is the viscous damping function. Here we rely on default model parameters, constants, and terms[††] as defined by [3,27].

$k-\omega$ model [1] introduces the following equations:

$$\underbrace{\frac{\partial(\bar{\rho}k)}{\partial t}}_{\text{transient term}} + \underbrace{\frac{\partial(\bar{\rho}\tilde{u}_j k)}{\partial x_j}}_{\text{convective term}} = \underbrace{\tau_{ij}\frac{\partial\tilde{u}_i}{x_j}}_{\text{production term}} - \underbrace{\beta_k\bar{\rho}\omega k}_{\text{dissipation term}} + \underbrace{\frac{\partial}{\partial x_j}\left[\left(\mu+\frac{\mu_t}{\sigma_k}\right)\frac{\partial k}{\partial x_j}\right]}_{\text{diffusionterm}} \tag{5}$$

$$\underbrace{\frac{\partial(\bar{\rho}\omega)}{\partial t}}_{\text{transient term}} + \underbrace{\frac{\partial(\bar{\rho}\tilde{u}_j\omega)}{\partial x_j}}_{\text{convectiveterm}} = \underbrace{\alpha\frac{\omega}{k}\tau_{ij}\frac{\partial\tilde{u}_i}{x_j}}_{\text{production term}} - \underbrace{\beta_\omega\bar{\rho}\omega^2}_{\text{dissipation term}} + \underbrace{\frac{\partial}{\partial x_j}\left[\left(\mu+\frac{\mu_t}{\sigma_\omega}\right)\frac{\partial\omega}{\partial x_j}\right]}_{\text{diffusion term}} \tag{6}$$

In the Menter SST model [2] for the ω equation, an extra term is considered in Eq. (6), which is called the cross-diffusion term:

$$\underbrace{2(1-F_1)\frac{\bar{\rho}\sigma_{\omega 2}}{\omega}\frac{\partial k}{\partial x_j}\frac{\partial\omega}{\partial x_j}}_{\text{cross-diffusion term}} \tag{7}$$

where we employ the same model parameters as in [1,2,32].

Further, we assume a calorically perfect gas and thus neglect high-enthalpy effects (perhaps the least applicable assumption but one that holds reasonably well at low hypersonic speeds [33]). We also neglect radiation heat transfer and exothermic/endothermic reactions due to the dissociation of the boundary layer. Focusing on high-level details of the turbulence models, the $k-\omega$ model captures energy convection and diffusion by incorporating the turbulent kinetic energy (TKE) k and the specific diffusion ω [1]. It shows better properties regarding the overestimation of shear stresses typically seen in the $k-\varepsilon$ model [34]. The SST formulation for the $k-\omega$ uses the $k-\omega$ turbulence model to operate in the viscous sublayer by leveraging its $k-\omega$ formulation in the inner portion of the boundary layer and has more inlet-independent properties in the freestream by exploiting the blending of the $k-\varepsilon$ model for the outer portion of the boundary layer [2]. Lastly (but by no means less important or relevant), the one-equation model proposed by Spalart and Allmaras [3] adds a single transport equation for a quantity used to modulate the artificial eddy viscosity.

Before conducting the present study, the main hypotheses regarding the performance of the individual models include the following:

1) The $k-\omega$ model and its derivatives would show a superior performance in the near-wall region.

2) The SA model should perform as well (or superior to) the other models in the outer portion of the boundary layer (in particular w.r.t. freestream parameters).

[††] We avoid restating all model parameters and constants because they are widely available in the literature.

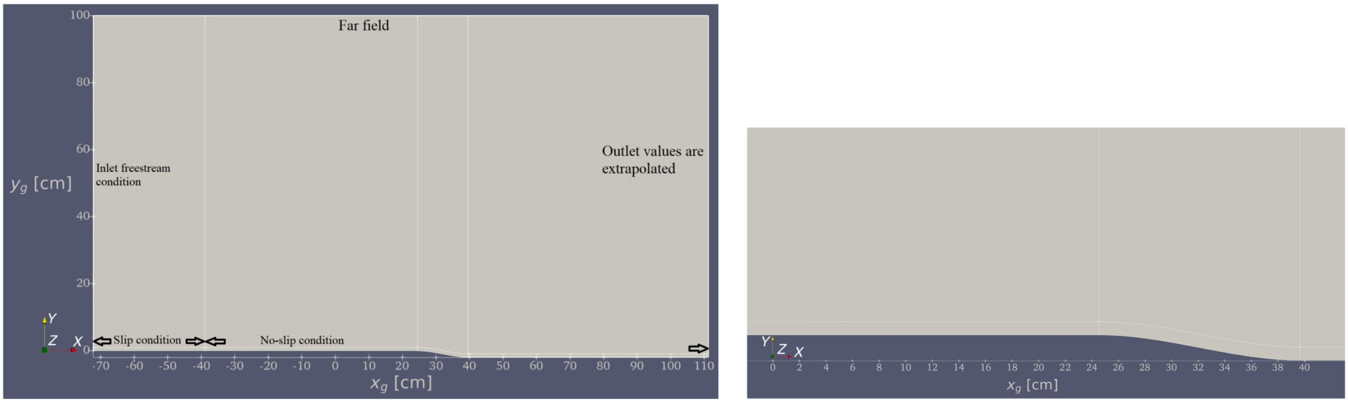

a) Full computational domain

b) Close-up of the zones of interests

Fig. 2 Schematic of the composite (ZPG+FPG+APG+ZPG) numerical domain.

Table 2 Boundary conditions

Condition	Value
Freestream Mach number	4.9
Pressure inlet gauge total pressure	2.345 MPa
Inlet supersonic/initial gauge pressure	4984.49 Pa
Inlet total temperature	380 K
Wall normal temperature gradient	0
Far field	$\partial/\partial y = 0$

3) The SST $k - \omega$ model should have an overall superiority due to its more robust formulation and ability to model the behavior of the boundary layer from the near-wall to the freestream region.

2. *Boundary Conditions*

The computational domain attempted to recreate the experimental setup as outlined by Tichenor et al. [4], which has been plotted in Fig. 1. Location 3 was not considered by [4] but is presented in the present work to assess the boundary layer distortion by both the strong FPG and APG regions. The domain has a freestream inlet followed by a bottom slip condition to ensure the numerically accurate capturing of the resulting shock wave at the edge. The inclined line of disturbances or Mach wave due to the presence of the flat plate edge is minimized and much better modeled by prescribing an upstream slip condition, as seen in Fig. 2. Downstream, a no-slip condition is imposed on the surface, whereas a far-field, zero-shear condition is imposed in the upper portion of the domain. The outlet values are extrapolated from the internal portion of the mesh to avoid an overconstrained system. The wall thermal boundary condition is a zero-gradient (a Neumann boundary condition) to ensure adiabatic wall conditions. Specific values for the aforementioned boundary conditions are presented in Table 2.

B. Inflow Condition Assessment and Boundary Conditions

As previously articulated, in the present work we reproduce the convex portion (identified as SPG) of Fig. 1. However, to accurately reproduce the incoming flow conditions for matching the reference boundary-layer thickness from experiments, we experimented on an auxiliary ZPG domain or flat plate with freestream inflow and slip conditions, as seen in Fig. 3. The selected turbulence model was the SA model due to its low computational cost and widespread use for external aerodynamics. Although priority was given to match the reference boundary-layer thickness at location 1 from experiments, we also looked at the wall velocity gradient (i.e., the friction velocity). Clearly, matching both boundary-layer parameters is not a trivial task and a tradeoff solution was chosen. It was estimated a streamwise length of 70 reference boundary-layer thicknesses ($\delta_{\mathrm{ref}} = 7.8$ mm, as reported by [4]) to vertically achieve δ_{ref} at location 1 (see Fig. 1) in our RANS predictions. We use as our streamwise reference location 1 as outlined in Fig. 1, and we report results with respect to the local body intrinsic coordinate system (i.e., curvilinear coordinates). Figure 4a depicts the grid point distribution in the fine mesh from Table 3. The whole computational domain dimensions are $235\delta_{\mathrm{ref}} \times 125\delta_{\mathrm{ref}}$ along the streamwise and wall-normal direction, respectively. We also took into account the shock wave at the leading edge and ensured that it did not caused any numerical artifacts in the far field or on location 1 (i.e., at $x/\delta_{\mathrm{ref}} = 0$ or $x_g = 15.9$ cm). To minimize the inclined shock generated at the edge of the flat surface (no-slip condition), an upstream zone with slip condition at the bottom was prescribed ($-112 < x/\delta_{\mathrm{ref}} < -70$). Figure 4b shows a close-up of the convex and concave curved wall. The zone of interest is about 20-δ_{ref}

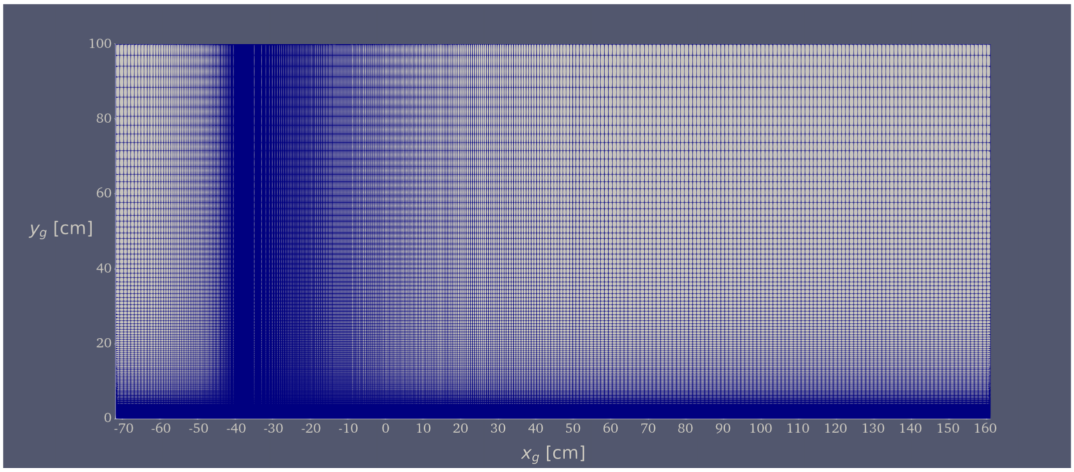

Fig. 3 Schematic of the auxiliary-ZPG numerical domain.

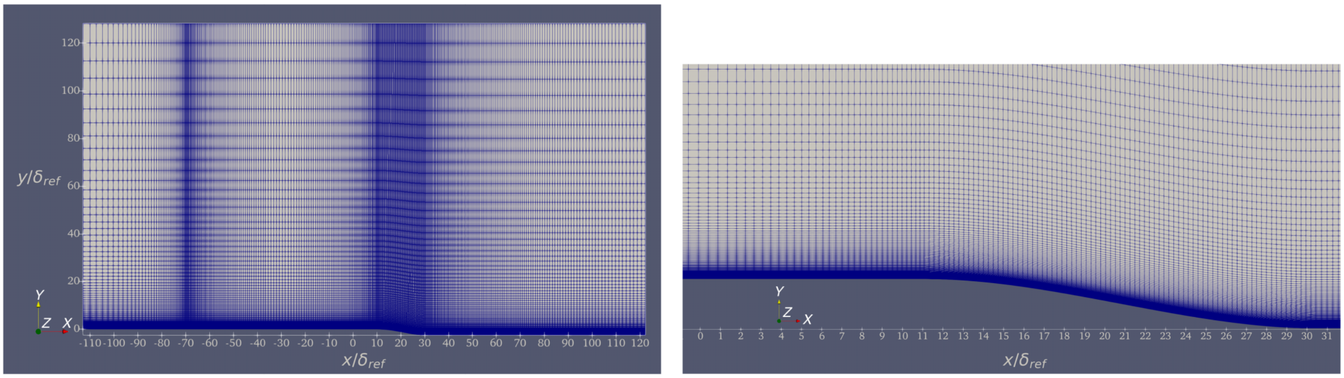

a) Full domain

b) Close-up of convex and concave surfaces

Fig. 4 Schematic of the grid point distribution in the fine mesh.

Table 3 Grid nomenclature

ID	Mesh dimensions ($s \times n$)
Coarse	95×50
Medium	190×100
Fine	380×200

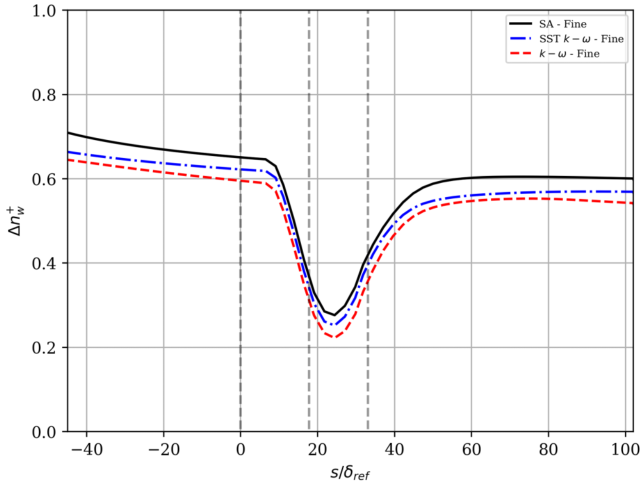

Fig. 5 Inner scaled off-wall resolution for the finest mesh. Vertical dashed lines correspond to locations 1, 2, and 3 (from left to right).

long, and special care has been taken to locally refine this curved geometry and to ensure clustering several points inside the viscous linear layer ($y^+ < 4$) of the turbulent boundary layer. Further, we bias the mesh toward the near-wall region to guarantee that the first off-wall node in wall units was located below one (i.e., $y^+ < 1$). We present the first off-wall node height for the fine mesh in Fig. 5.

The geometry has a moderate curvature as characterized by δ_{local}/R that takes a peak value of 0.041 (location 2 at $x/\delta_{\text{ref}} = 17.8$ or $x_g = 29.8$ cm) in the convex region and −0.055 in the concave region. Interestingly, both peak values for δ_{local}/R do not coincide with the peak pressure gradient values. In fact, the streamwise distance between the peak FPG and the peak δ_{local}/R is approximately 4–5δ's for the convex surface. Furthermore, that distance shrinks to 2–3δ's between the peak APG and the minimum δ_{local}/R in the concave surface. More details will be supplied later in this paper. The surface is modeled using a single curve following Tichenor et al. [4], i.e., $y = A(x - x_1)^3 + B(x - x_1)^2$, where A and B are the polynomial coefficients, x indicates the location of interest, and x_1 is the axial location where the curvature begins. We used Eq. (8) to calculate the radius of curvature along the wall curvature with A, B, and x_1 corresponding to the values published by Tichenor et al. [4]. We chose location 3 (at $x/\delta_{\text{ref}} = 33.2$ or $x_g = 41.8$ cm) to coincide with the peak APG value that falls just off the concave section, one notable distinction for the present work as compared with the reproduced diagram from [4] in Fig. 1.

$$R = \frac{\left[1 + (dy/dx)^2\right]^{3/2}}{|d^2y/dx^2|} = \frac{((3A(x - x_1)^2 + 2B(x - x_1))^2 + 1)^{1.5}}{|6A(x - x_1) + 2B|} \tag{8}$$

We reproduce a limited set of results from the available literature in the present work to provide a baseline for validating and contrasting our results and conclusions. The reference cases are mentioned in Table 4 and are consistently outlined in the legends. Further, we

Table 4 Reference cases (values from the present work are averaged among the three considered models)

Reference	PG	Source	$Re_{\delta 2,\text{inc}}$	$Re_{\delta 2,\text{comp}}$	Ma_∞
Tichenor et al. [4]	ZPG	Exp.	9,000	Not available (~3,895.5)	4.9
Tichenor et al. [4]	FPG	Exp.	13,000	Not available (~5,626.8)	4.9
Neeb et al. [5]	ZPG	Exp.	Not available (~1,467)	635	5.03
Neeb et al. [5]	ZPG	Exp.	Not available (~1,700)	736	5.59
Neeb et al. [5]	ZPG	Exp.	Not available (~1,774)	768	5.36
Neeb et al. [5]	ZPG	Exp.	Not available (~1,795)	777	5.33
Araya and Jansen [8]	ZPG	DNS	9,592	4,854	5
Araya et al. [6]	ZPG	DNS	1,633.4	790	5
Nicholson et al. [7]	ZPG	DNS	8,221	4,021	4.9
Nicholson et al. [7]	FPG	DNS	14,763	6,464	4.9
Present work—location 1	ZPG	RANS	~7,622	~3,300	4.9
Present work—location 2	FPG	RANS	~10,295	~2,340	4.9
Present work—location 3	APG	RANS	~5,783	~3,913	4.9

Values that were not available were estimated based on the ratios calculated and presented in Fig. 17c. Exp. = Experiment.

discriminate among compressible and incompressible flow parameters where appropriate. Any flow parameter without a subscript is assumed to be compressible unless otherwise stated.

C. Grid Independence Test

To assess the independence of our results from the discretization, we performed a grid independence test and compared the numerical results with experimental results by Tichenor et al. [4]. Initially, we assess the ability of the models to predict the boundary-layer thickness growth independent of the mesh resolution as seen in Fig. 6. Here, the boundary-layer thicknesses are computed from the streamwise velocity profiles based on a 99% freestream velocity, U_e, criterion. The SA model exhibits a large degree of resilience against changes in the mesh. This was consistent throughout the different quantities used to assess grid independence. In the boundary-layer thickness, all models follow the same tendency although differing on the predicted magnitude by up to 32% (about 2 mm). Furthermore, all turbulence models have predicted the typical linear growth of δ in canonical or ZPG turbulent boundary layers. The SA model has the best agreement with the experimental data; nonetheless, this was somehow expected because it was used to estimate the development region from the flat plate edge. The different turbulence models considered in the present study share the same principal domain; still, all flow parameters are further normalized based on the local boundary-layer thickness. The observed underprediction of δ (small in the ZPG region but mild in the FPG region) might be due to a mismatch in our interpretation of the data provided by [4] or a delayed growth predicted by the SA model.

The skin friction was indirectly verified through the friction velocity shown in Fig. 7. The standard base $k-\omega$ model has a superior performance in the SPG region when comparing against the experimental data. Further, the SA model's lack of sensitivity to mesh variations is reinforced by a near perfect collapse of all mesh results.

Furthermore, we also investigate grid independence for the streamwise velocity profiles. All models exhibit a remarkable collapsing level at the three locations and meshes considered, as shown in Fig. 8. When compared with experiments by [4,5] and DNS by [6–8] at a similar Mach number of 5, all turbulence models tend to slightly underpredict the streamwise velocity in the outer part of the boundary layer at location 1 (ZPG) (i.e., for $n/\delta > 0.05$). Note that data from Neeb et al. [5] and Araya et al. [6] are at much lower Reynolds numbers. The Reynolds number dependency is described as a local flow deceleration in the buffer layer ($n/\delta \approx 0.05$) at lower Reynolds numbers when outer units are employed. As the hypersonic flow accelerates in the convex region (location 2) due to FPG, the increased wall velocity slope is obvious, generating larger values of the friction velocity (as discussed in Fig. 7). All turbulence models exhibit a fair agreement in the inner region with DNS by Nicholson et al. [7] under similar geometrical and flow conditions as in [4]. Focusing our attention on the logarithmic zone of the boundary layer (i.e., $0.15 < n/\delta < 0.4$), while the SA and $k-\omega$ models display better agreement with DNS by [7], SST results approach Tichenor's experiments. The wake region above the log zone ($n/\delta > 0.4$) is characterized by a good collapsing of all models with DNS by [7]. Overall, there is not a discernible supremacy of any of the three models, which depends on the streamwise and wall-normal location considered. That being said, grid independence is clearly seen from the aforementioned results, including location 3 (APG) where flow strongly decelerates in the zone $0.1 < n/\delta < 0.4$.

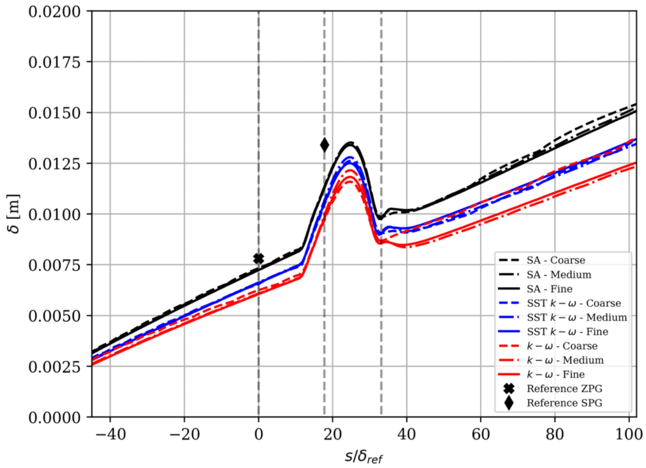

Fig. 6 Momentum boundary-layer thickness. Reference points are reproduced from Tichenor et al. [4]. Vertical dashed lines correspond to locations 1, 2, and 3 (from left to right).

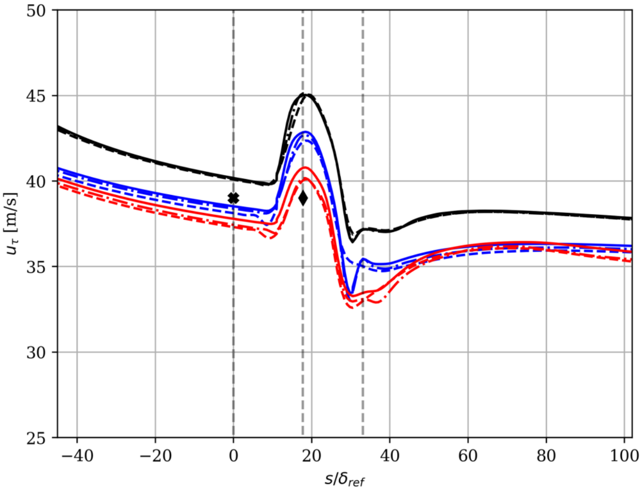

Fig. 7 Friction velocity. Reference points are reproduced from Tichenor et al. [4]. Same legend as in Fig. 6. Vertical dashed lines correspond to locations 1, 2, and 3 (from left to right).

The relative turbulent viscosity also provides some insight into the underlying modeling assumptions introduced by the previously mentioned closure models. Figure 9 shows the relative eddy viscosity, ν_T/ν_∞, for all models and meshes considered for the present study at the three streamwise stations: location 1 (ZPG), location 2 (FPG), and location 3 (APG). In general, the SA model and both SST models exhibit a higher peak value when compared with the base $k-\omega$ model, particularly at locations 1 and 2. Note that the eddy viscosity can be up to three orders of magnitude larger than the molecular viscosity at $n/\delta \approx 0.4$–0.5. The predicted values of ν_T/ν_∞ in the APG zone (location 3) are much larger in the one-equation model (i.e., SA) in comparison with two-equation models, up to 50% larger in peak value. It is important to highlight that the SST model [2] has been developed in order to operate well under flow deceleration or the presence of APG. In the near-wall region, the SA model has generated the largest eddy viscosity values. Although peak values of ν_T/ν_∞ are located around 40–50% of the boundary-layer thickness in the ZPG region, there is an evident displacement of these peaks toward the edge of the boundary layer (60–80% of δ) in the convex surface or location 2. This phenomenon has also been observed in the concave surface or location 3. Notice the nonnegligible level of ν_T/ν_∞ intensity outside the boundary-layer thickness in the convex and concave region. Moreover, one cannot state that turbulence is enhanced, due to either favorable or adverse pressure gradient (APG), near the edge of the boundary layer if high values of ν_T/ν_∞ are present, because turbulent mixing (i.e., Reynolds shear stresses) is also dependent on the local streamwise velocity slope ($\partial U/\partial n$). The modeled Reynolds shear stresses are discussed in the next section to address the previous statement. The bottom line of the grid independence study is as follows: i) a consistent trend of all medium-mesh results to approximate results from the fine meshes was observed; ii) the SA model has shown to possess a great insensitivity to grid resolution, and all results have nearly collapsed; and iii) according to previous conclusions, outcomes discussed in Sec. III and beyond will be based on the fine-mesh simulations.

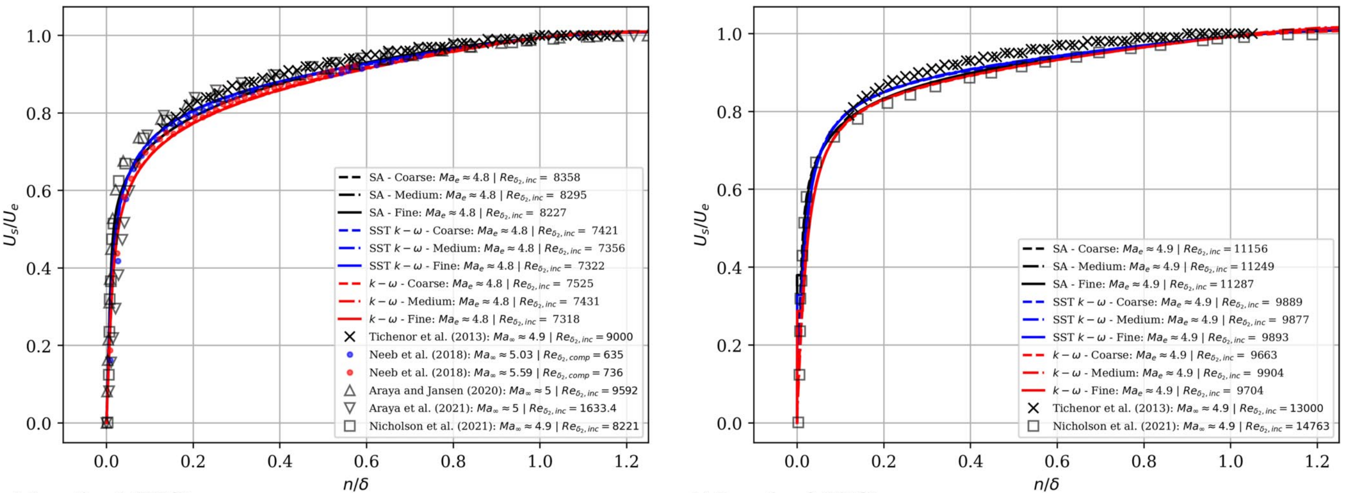

a) Location 1 (ZPG)

b) Location 2 (FPG)

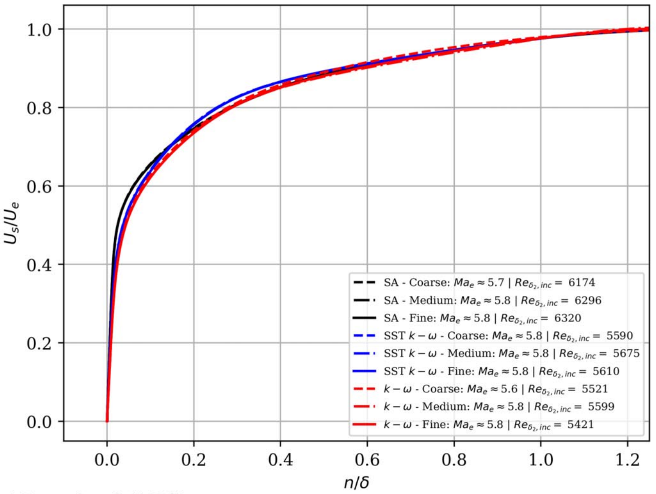

c) Location 3 (APG)

Fig. 8 Outer-scaled velocity profiles. Reference points are reproduced from Tichenor et al. [4].

D. Flow Visualization

All results present in this section correspond to the fine mesh and the SA turbulence model. Contours of the local Mach number are plotted in Fig. 10. The full domain can be seen in Fig. 10a. A very weak inclined line of disturbances is observed at approximately 11.3° with respect to the x direction, very close to the Mach angle μ ($= \sin^{-1}(1/M_\infty)$), which is generated at the edge of the flat surface at $x/\delta_{\text{ref}} = -70$. As expected, the hypersonic flow went through a strong acceleration in the convex surface curvature region due to the presence of FPG. The expansion waves end up in a well-defined compression wave due to the change in wall curvature condition imposed in our computational domain, in such a way the flow returns to its incoming ZPG conditions. The family of compression waves generated by each point along the concave surface finally merged outside the turbulent boundary layer, as can be seen in Fig. 10b. The inclination of the compression shock caused by the concave curvature was estimated to be around 7.7°. It is worth highlighting that both types of waves are fully convected in the outflow plane. The top boundary has been prescribed far enough to avoid any interference on the bottom wall-bounded flow or to evade the shock wave reflection from the top region back to the domain. The y component of the velocity V significantly increases as the hypersonic flow expands through the convex wall surface, as seen in Fig. 11. The principal components of the x-y strain rates, i.e., $\partial U/\partial y$ and $\partial V/\partial x$, are plotted in Fig. 12, respectively. Both components are normalized by $\delta_{\text{ref}}/U_\infty$, i.e., flow parameters at location 1. Clearly, the positive component $\partial U/\partial y$ is significantly much larger than $\partial V/\partial x$ (more than one order of magnitude larger), mostly concentrated in the turbulent boundary layer with negligible values across the expansion waves and some slight values in the compression wave zone. The expansion waves at the beginning of the convex wall surface are described by the presence of high (negative) values of $\partial V/\partial x$ because V increases in a negative manner, as previously discussed in Fig. 11. It is important to highlight that the convex curvature causes a downward movement of the flow, concentrating large negative values of the strain rates due to the $\partial V/\partial x$ component in the near-wall region of the turbulent boundary layer. This is consistent with what was reported by Tichenor et al. [4] in their Fig. 4b. On the other hand, a streamwise acceleration of V can be observed across the compression waves due to the secondary concave curvature. Figure 13 depicts the principal components of the bulk dilation ($\partial U/\partial x$ and $\partial V/\partial y$, respectively) normalized by $\delta_{\text{ref}}/U_\infty$, as well. There is a significant growing streamwise acceleration of U in the near-wall region of the boundary layer from the beginning of the convex region to the concave surface end. Furthermore, the $\partial V/\partial y$ exhibits a change in sign in the inner region of the boundary layer. For instance, at location 2 in the convex surface, negative values of $\partial V/\partial y$ were observed for $y/\delta < 0.1$, whereas the contrary occurs for $y/\delta > 0.1$. The in-plane bulk dilatation ($\partial U/\partial x + \partial V/\partial y$) remains positive inside and outside the boundary layer until the end of the convex surface (i.e., $x/\delta_{\text{ref}} \approx 25$) and beginning of the concave curvature. Because both components $\partial U/\partial x$ and $\partial V/\partial y$ are positive beyond $y/\delta \approx 0.1$, it can be inferred that bulk dilatation plays an important role as extra strain in the outer part of the turbulent boundary layer, which is consistent with studies by Tichenor et al. [4] and Dussauge and Gaviglio [35]. The family of compression waves emitted by each point of the concave curvature is

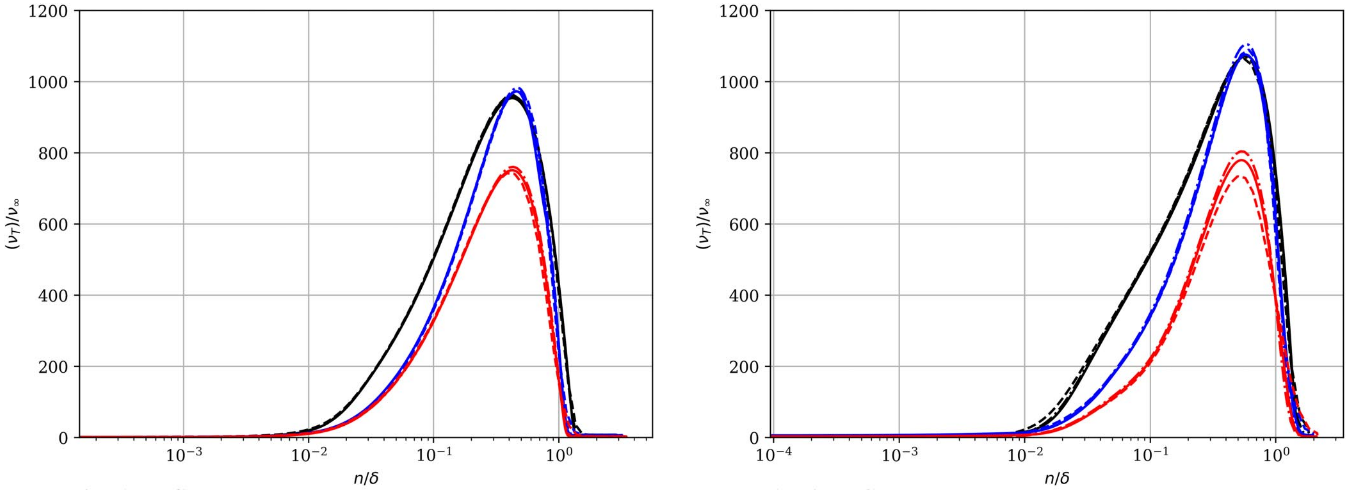

a) Location 1 (ZPG)

b) Location 2 (FPG)

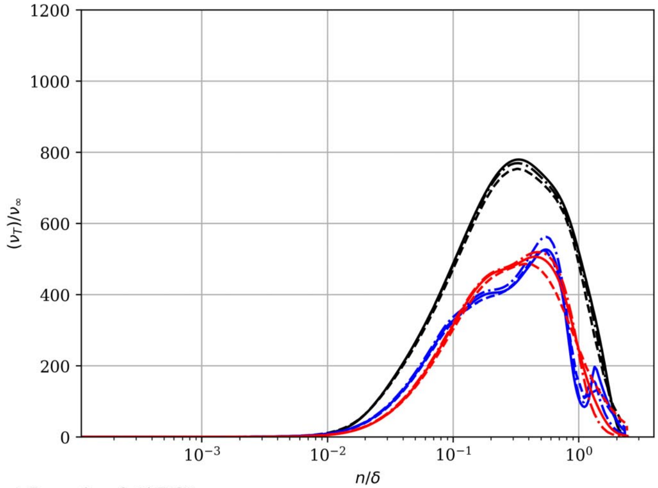

c) Location 3 (APG)

Fig. 9 Relative turbulent eddy viscosity. Same legend as in Fig. 6.

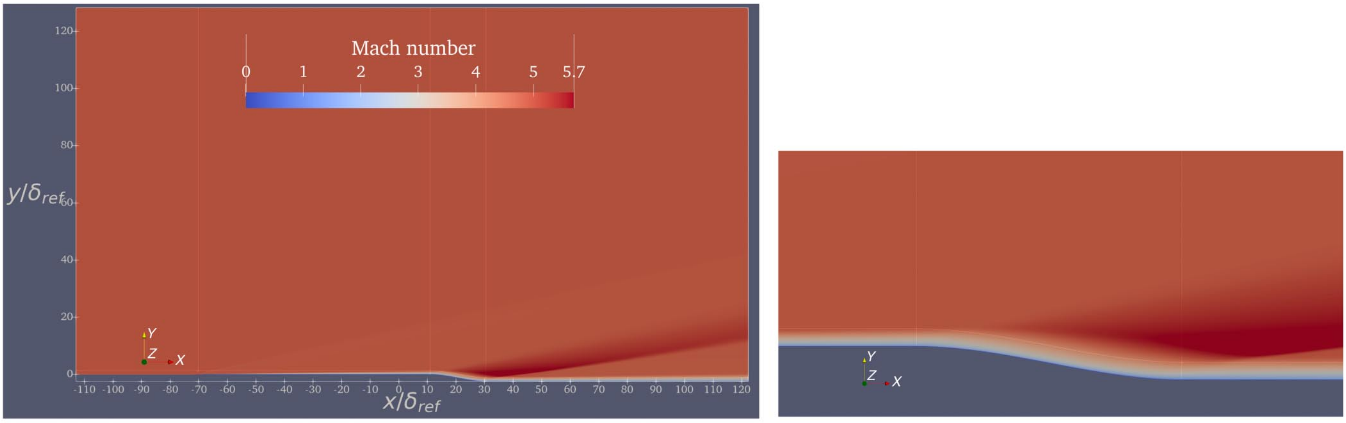

a) Full domain

b) Close-up of convex surface

Fig. 10 Isocontours of the Mach number.

clearly identified by significant negative values of $\partial V/\partial y$. All waves finally merged in one clear-cut compression shock in the outer inviscid region.

III. Numerical Solution and Discussion

In this section, we show and discuss the major features of mean streamwise velocity, compressibility effect on the Reynolds number, pressure gradient influence, mean thermal profiles, Reynolds shear stresses, and some boundary-layer parameters for the fine mesh results. Furthermore, the principal terms of the turbulent transport equations, such as production and dissipation of k and ω, are analyzed. Although the major focus of this study consists of evaluating how a canonical ZPG turbulent hypersonic boundary layer (location 1) is distorted when subjected to a convex wall curvature (location 2), a secondary objective, but still important goal, is the assessment of APG caused by the concave wall curvature (location 3).

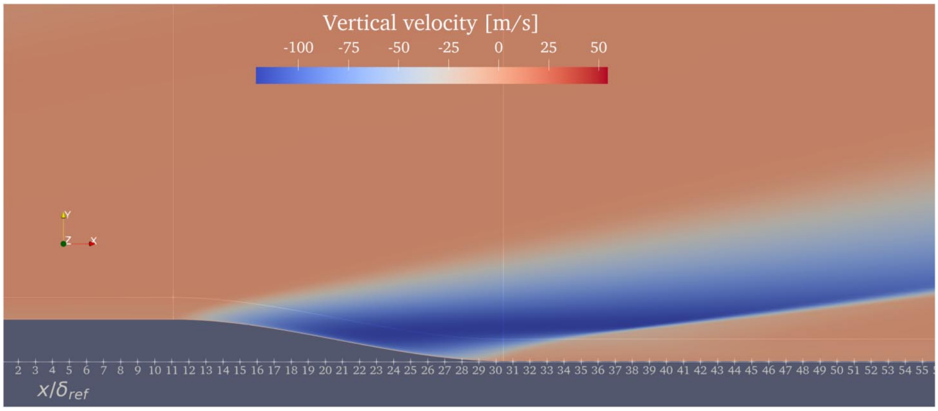

Fig. 11 Vertical velocity V.

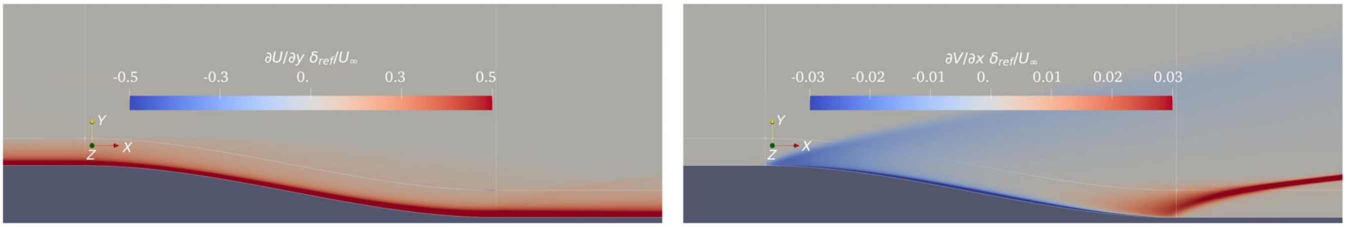

a) Normalized $\partial U/\partial y$

b) Normalized $\partial U/\partial x$

Fig. 12 Isocontours of principal strain rate components.

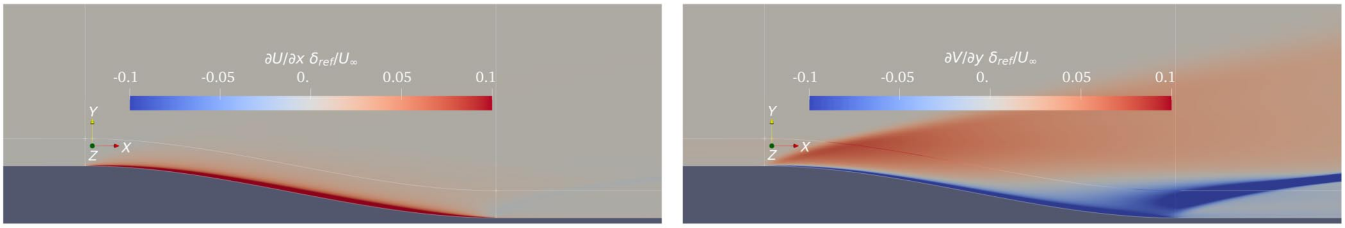

a) Normalized $\partial U/\partial x$

b) Normalized $\partial U/\partial y$

Fig. 13 Isocontours of bulk dilatation components.

A. Velocity Profiles

We first studied the behavior of the edge velocity for all the models to assess their freestream behavior. The edge velocity can be obtained by first calculating U_{99} and approximating the distance through a first-order Taylor expansion on the velocity profile as a function of wall-normal distance. These results are presented in Fig. 14. The SA model has an odd dip in the hypersonic convex expansion that seems rather unphysical due to the expected flow acceleration resulting from the expansion. The SST $k-\omega$ has a small plateau before continuing to accelerate toward the same peak velocity predicted by the base $k-\omega$ model. For the APG region, the base $k-\omega$ and SST $k-\omega$ collapse to the same value, a slightly lower value than that predicted by the SA model. The edge Mach number is shown in Fig. 14b with similar trend as U_e. The flow is accelerated to a maximum Ma_e of roughly 5.9 (20% increase) after nearly 24-δ_{ref} from the convex curvature beginning. This may be attributable to the sudden cooling of the boundary layer at the expansion; thus, the sound speed decreases. There is a temperature increase at the boundary layer's edge in the order of 40% from the coldest point throughout the FPG and the most downstream ZPG (not shown). It is worth noting that the temperature at the boundary-layer edge is hotter after the convex–concave surfaces than the incoming freestream by 3%.

The combined effects of the thermal/flow boundary layers and compressibility effects can be characterized by the local Mach number. Thus, we present the wall-normal profiles of the local Mach number (normalized by the edge value) at the three locations in Fig. 15. In general, all models tend to follow a similar behavior with very little spread in their predicted local Mach number. However, an 18–20% increase in the local peak Mach number ($Ma \approx 6$) was observed in the APG (not shown). The SA model consistently predicts higher values throughout the curved wall and the flat section that follows. For the incoming ZPG flow, all models tend to underpredict the local Mach number, as compared with DNS by [6,8] and experimental data by [5] at $Ma \approx 5$. This underprediction is the largest (~15%) for the $k-\omega$ model. Although the magnitude is underpredicted, the overall slope and shape of the profiles (for the ZPG region) is well captured by turbulence models.

We then computed the van Driest transformed velocity to assess the distortion of the boundary layer while accounting for density variations throughout the boundary layer. The van Driest transformation integral was implemented as a cumulative trapezoid numerical integration scheme. To validate the incoming ZPG flow conditions, we compare in Fig. 16a the present numerical solutions with experimental data from Tichenor et al. [4], DNS data from Duan et al. [36], DNS data from Araya et al. [6] (although at lower Re), DNS data from

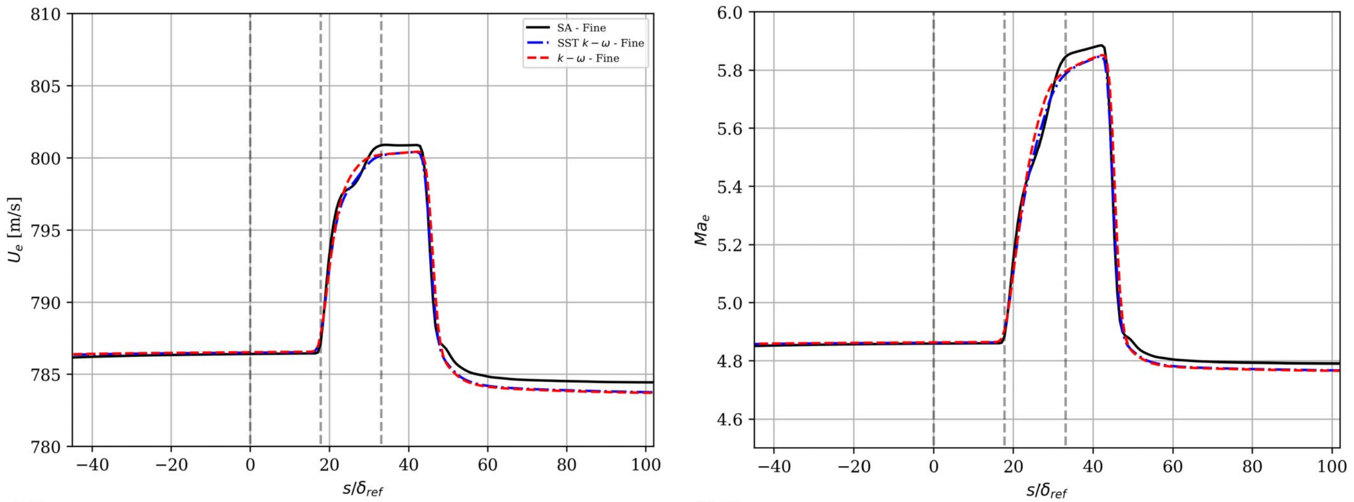

a) U_e

b) Ma_e

Fig. 14 Streamwise evolution of a) the edge velocity U_e, and b) Mach number Ma_e. Vertical dashed lines correspond to locations 1, 2, and 3 (from left to right).

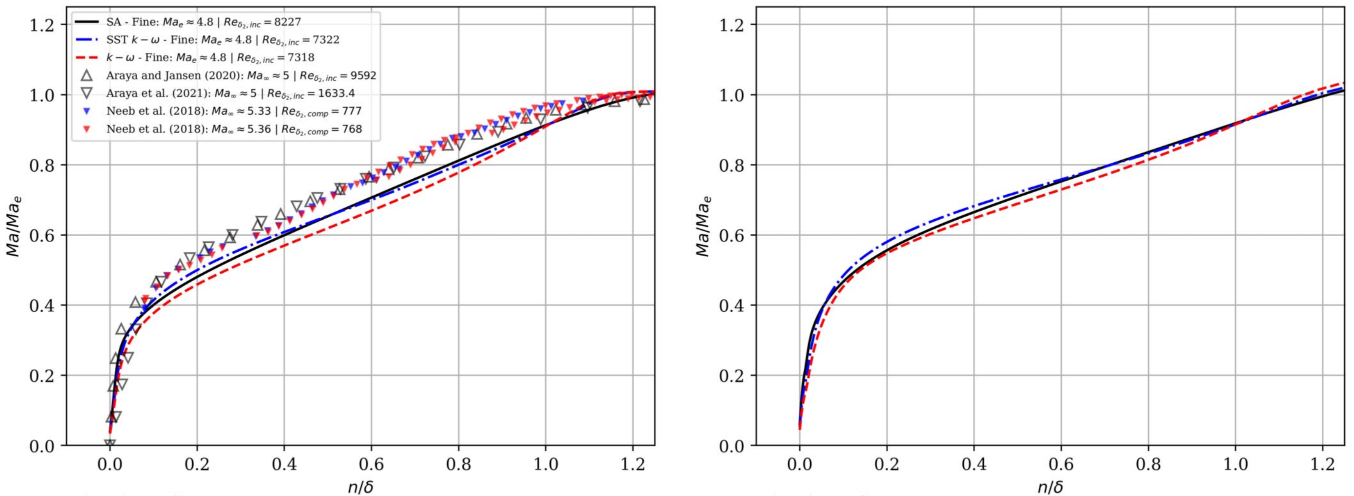

a) Location 1 (ZPG)

b) Location 2 (FPG)

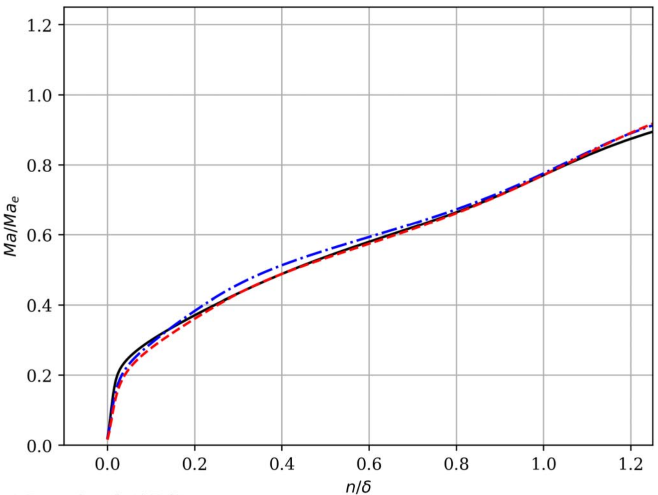

c) Location 3 (APG)

Fig. 15 Wall-normal Mach number profiles.

Araya and Jansen [8], DNS data from Nicholson et al. [7] (also for location 2), two log laws [37–39], and the composite profile proposed by Reichardt and Finley as reported by Guarini et al. [40]. The SA model has a slight dip in the log region when contrasted with the $k-\omega$ variants. The classical log law proposed by Osterlund et al. [37] has a better agreement with the slope in the log region; however, the intersect is better captured by the variant proposed by Fernholz and Finley [38]. The experimental data points from [4] fall between the SST $k-\omega$ and SA in the outer portion of the boundary layer. In contrast, the wake region exhibits better agreement with the SST

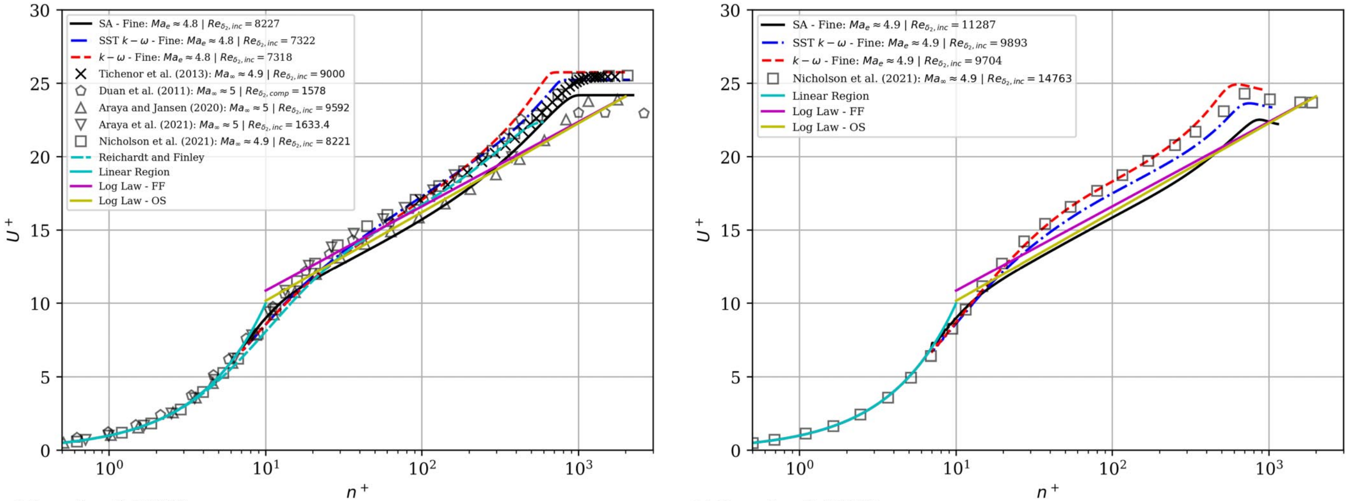

a) Location 1 (ZPG) **b) Location 2 (FPG)**

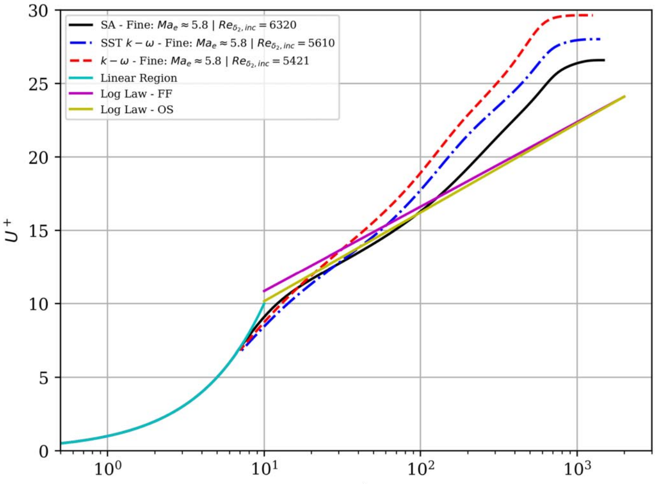

c) Location 3 (APG)

Fig. 16 Van Driest–transformed velocity profile. Reference points are reproduced from Tichenor et al. [4]

$k-\omega$ and the base $k-\omega$. The log region is significantly longer in the FPG region (location 2), and a better agreement with the slope proposed by Fernholz and Finley [38] can be seen. The base $k-\omega$ model also exhibits better agreement with the DNS data by Nicholson et al. [7] throughout the log and outer regions. This agreement breaks down nearing the wake region where the validation data fall between the base and SST $k-\omega$ variants. However, velocity profiles fall above the log law by [38]. Again, the SA model is the outlier among all models considered in the present study with lower values compared with the predictions made by the three $k-\omega$ variants. Nevertheless, the changes of the boundary layer are lower in the FPG region as compared with the APG region, where an obvious distortion of the log (note the presence of a secondary steeper log slope for $n^+ > 100$) and wake region are observed. In addition, there is a spread among all models in the APG region with the SST variants having the closest agreement. The stronger distortion caused by the APG over the FPG is clear when compared against the baseline ZPG region.

B. Reynolds Number Compressibility Dependence

The compressibility effects on Re_{δ_2} are also explored on Fig. 17. Tichenor et al. [4] presents Re_{δ_2} without accounting for density variations due to experimental limitations. The incompressible Re_{δ_2} in Fig. 17a differs by 15% at location 2 when comparing the SA model to the aforementioned experimental data. A notable difference when accounting for compressibility effects in Fig. 17b is the location for the peak Reynolds number that shifts from the vicinity of location 2 to the downstream vicinity of location 3. The lowest predicted values are consistently from the base $k-\omega$. The SST $k-\omega$ and the base $k-\omega$ collapse fairly well throughout the first ZPG portion before an interesting shift as they slightly diverge throughout the second ZPG portion. Figure 17c highlights the ratio of the incompressible to the compressible $Re_{\delta 2}$, which peaks at location 2 and reaches unity just after the highest APG location. Throughout ZPG regions, it remains mostly constant due to the lack of streamline curvature effects.

C. Pressure Gradient Assessment

The streamline curvature effects are directly related to the strength of the resulting pressure gradients. To assess their strength, we studied the wall pressure evolution and the boundary-layer pressure gradient as presented in Fig. 18 where reference points are reproduced from Tichenor et al. [4]. The vertical dashed lines correspond to the maximum and minimum pressure gradient locations. The considered turbulence models have an excellent agreement on both the wall pressure distribution and the streamline pressure gradient. The peak reduction in wall pressure corresponds to roughly 65–68% of the incoming ZPG value. Although Tichenor et al. [4] focused solely on the effect of the supersonic expansion due to convex streamline curvature, we have observed a stronger pressure gradient induced by the concave surface that follows the convex corner. Following this compression, the wall pressure returns to values just under the incoming flow (98–99%). In Fig. 18b, the streamwise variation of the edge pressure P with respect to the curvilinear coordinate s is depicted (left axis) as well as the wall curvature

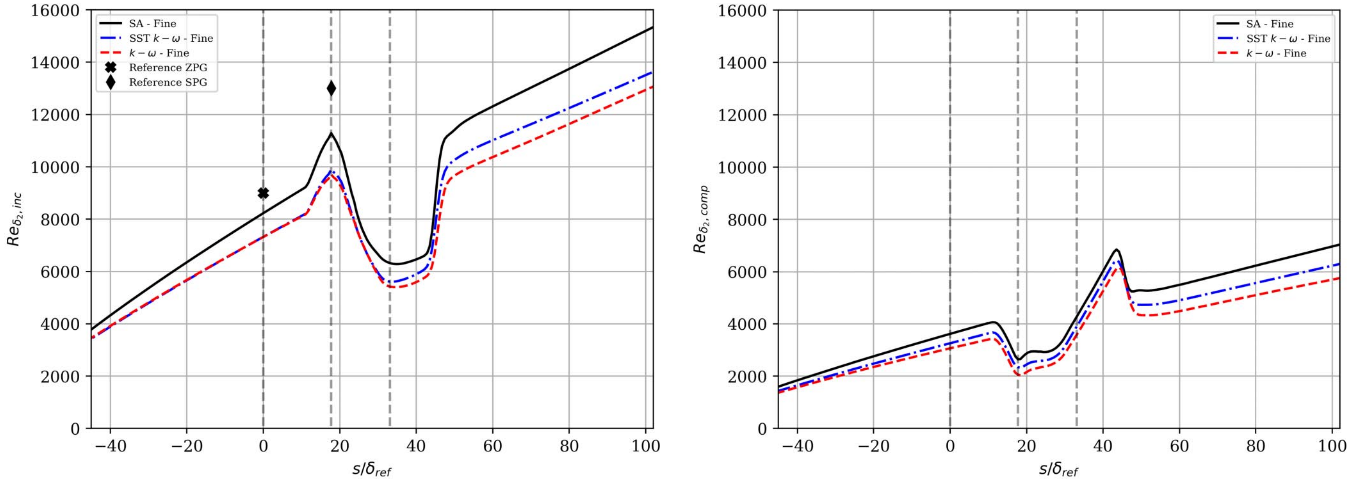

a) Without compressibility correction

b) With compresibility correction

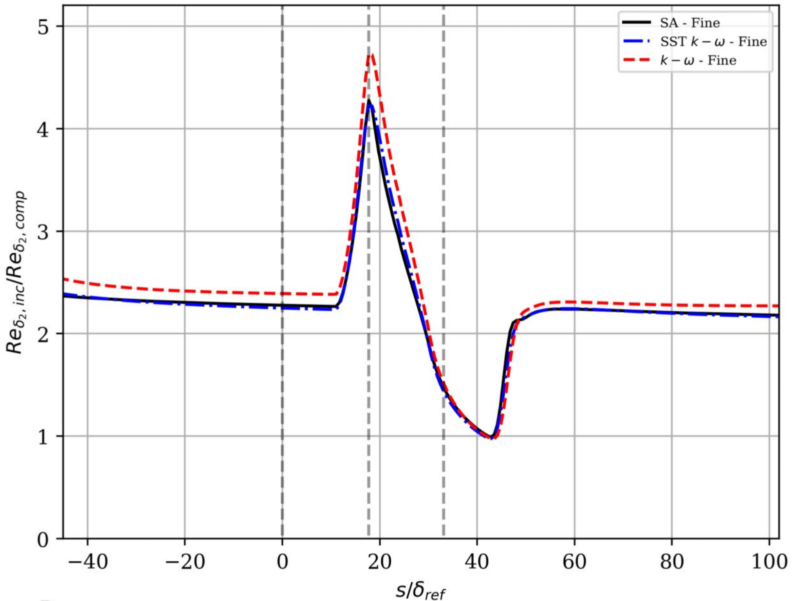

c) $\frac{Re_{\delta 2,\,inc}}{Re_{\delta 2,\,comp}}$

Fig. 17 Momentum thickness Reynolds number Re_{δ_2}. Reference points as in the work of Tichenor et al. [4]. Vertical dashed lines correspond to locations 1, 2, and 3 (from left to right).

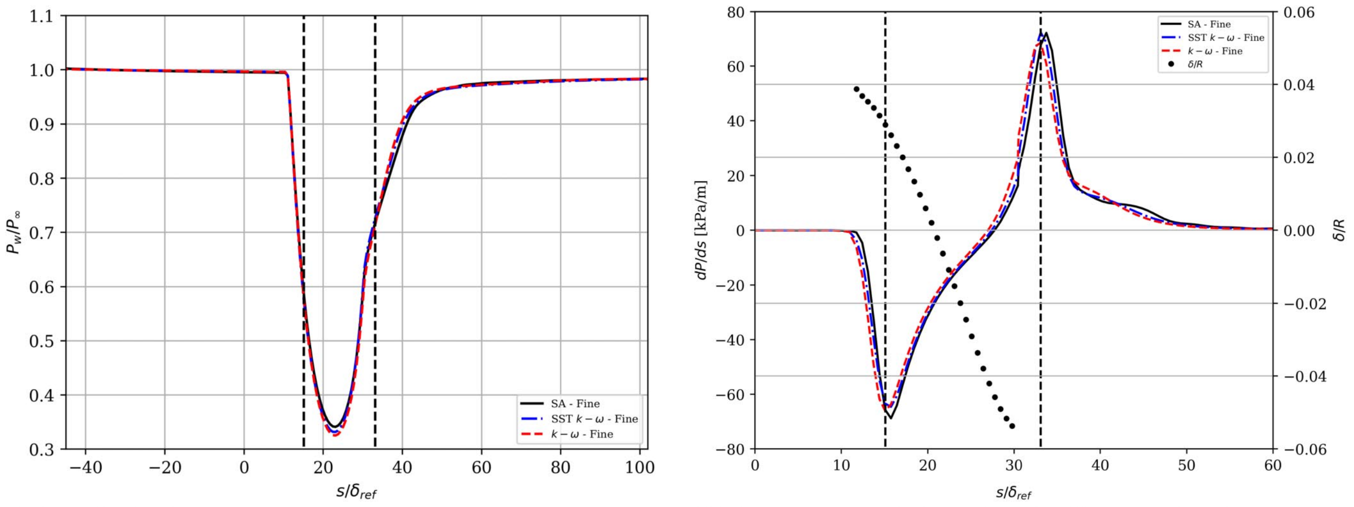

a) Normalized wall pressure

b) Edge pressure gradient and the ratio of local boundary layer thickness to radius of curvature

Fig. 18 Pressure evolution visualized in terms of normalized wall pressure and pressure gradient alongside δ/R.

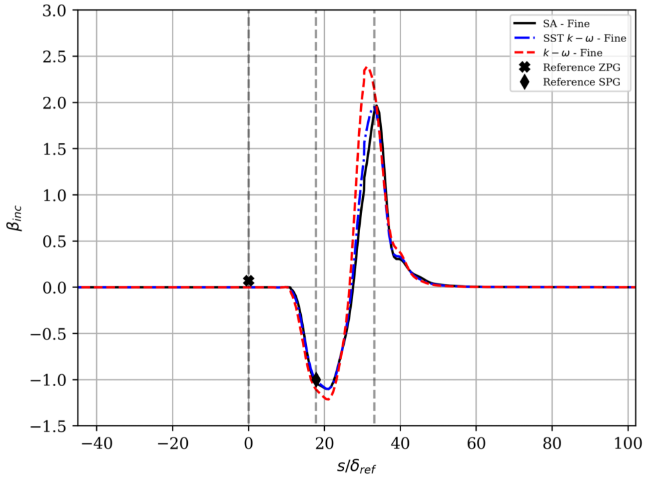

Fig. 19 Clauser's pressure parameter. Reference points are reproduced from Tichenor et al. [4]. Vertical dashed lines correspond to locations 1, 2, and 3 (from left to right).

parameter δ/R, where δ is the local boundary-layer thickness and R is the local curvature radius as computed by Eq. (8). According to the review paper by Simpson [41], strong wall curvatures are considered to be in the order of $|\delta/R| \approx 0.1$. Because the corresponding maximum value of δ/R in the convex region was 0.041 and in the concave region was −0.055, as articulated in Sec. II.B, we can state that present prescribed curvatures are moderate. In fact, we have noted a delay or shift between the location of the maximum absolute values of wall curvature and streamline pressure gradient: the maximum of $|dP/ds|$ occurs downstream of $|\delta/R|_{\max}$ location. What is more, the location 3 was selected for APG assessment due to the maximum $|dP/ds|$ occurrence; however, the local wall curvature is zero.

Another parameter characterizing the strength of the pressure gradient is the Clauser's pressure parameter, $\beta = (\delta^*/\tau_w)(dP/ds)$ [42]. We report values for β based on the incompressible displacement thickness to compare against the available experimental data [4]. As seen from Fig. 19, the agreement with experimental results is fairly notable.

D. Walz Equation

Alfred Walz proposed a relationship for relating the temperature and flow boundary layers, which has been historically known as the Walz's equation [43]. The relationship proposed by Walz did not account for pressure gradients, and its applicability has typically been limited to ZPG regions with adiabatic wall conditions. Recently, a modified relationship between the thermal and flow boundary layers has been proposed by Zhang et al. based on a generalized Reynolds analogy (GRA) [44]. GRA accounts for additional factors that increase its applicability to additional wall-bounded flows, i.e., at different Prandtl numbers, wall temperatures, Mach numbers, Reynolds numbers, and pressure gradients. In Fig. 20, we compare the present numerical solutions with experimental data from

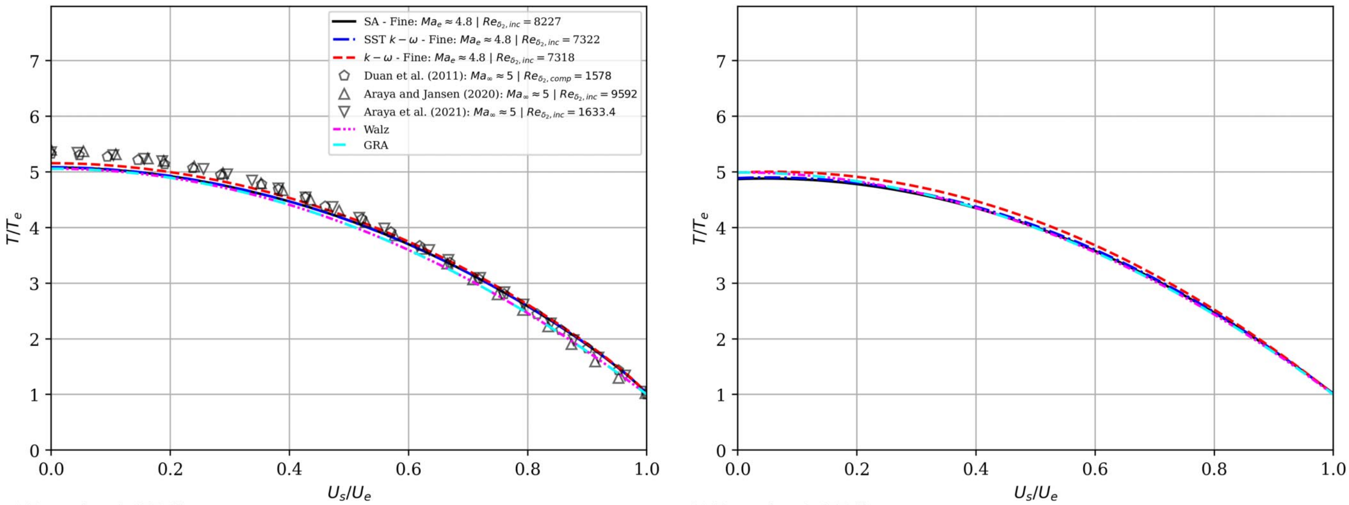

a) Location 1 (ZPG) **b) Location 2 (FPG)**

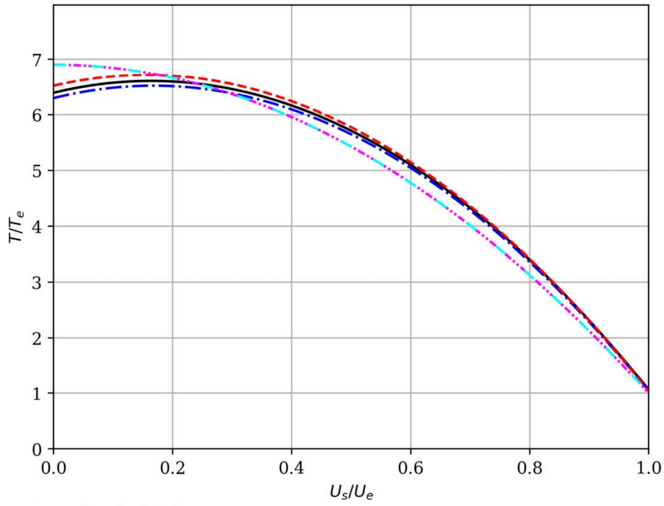

c) Location 3 (APG)

Fig. 20 Walz equation [43] and the generalized Reynolds analogy (GRA) [44].

Table 5 Summary of errors for the Walz and generalized Reynolds analogy

Model—location	Maximum error, %	Minimum error, %	Mean error, %	RMS, %
SA—Loc. 1	5.35	0.004	3.34	3.71
SA—Loc. 2	2.43	0.001	1.26	1.15
SA—Loc. 3	8.81	0.006	5.07	6.09
SST $k-\omega$—Loc. 1	5.67	0.008	3.53	3.91
SST $k-\omega$—Loc. 2	2.07	0.000	1.23	1.26
SST $k-\omega$—Loc. 3	8.25	0.002	4.85	5.42
$k-\omega$—Loc. 1	6.59	0.008	4.12	4.55
$k-\omega$—Loc. 2	3.96	0.657	2.96	2.76
$k-\omega$—Loc. 3	9.79	0.006	5.99	6.35

Tichenor et al. [4], DNS data from Duan et al. [36], DNS data from Araya et al. [6], Walz's equation, and the GRA. Further reinforcing our previous findings, we see a significantly larger distortion of the boundary layer in the APG region, whereas the FPG region suffers very little. In fact, Walz's equation provides a fairly accurate prediction of the results observed in location 2 and the thermal-flow boundary-layer interaction at location 3 when using local parameters for the recovery temperature. The GRA relationship collapses with Walz's equation, a remarkable feat by the GRA model given that the recovery temperature predicted by GRA matches the recovery temperature calculated by RANS. Both the GRA and Walz equations are solved three times, one for each model, and the results shown in Fig. 20 are the average.

Visually judging the performance of Walz's equation and the GRA can be challenging from Fig. 20. Thus, we present a summary of errors in Table 5. We present the maximum, minimum, and mean error between the three closure models and both theoretical predictions. Further, we present the root mean square [RMS; see Eq.(9)] to illustrate the variance of errors that is not captured by the other metrics. For location 1 (ZPG), the best performance is obtained by the SA model as per the cumulative error and the peak error observed. At location 2, i.e., the FPG region, the SST $k-\omega$ models yield a superior performance. The SST $k-\omega$ models also has the upper hand at location 3 as per the peak and cumulative errors.

$$\mathrm{RMS} = \sqrt{N_y^{-1} \sum \left(\frac{((T/T_e)_{\mathrm{RANS}} - (T/T_e)_{\mathrm{GRA}})^2}{(T/T_e)_{\mathrm{GRA}}^2} \right)} \tag{9}$$

E. Reynolds Shear Stresses

A fundamental motivation behind closure models is to approximate Reynolds stresses. The Favre averaging procedure applied to Eq. (2) generated the extra convective term

$$\tau_{ij}^R = -\overline{\rho u_i' u_j'} \tag{10}$$

which is the Favre-averaged Reynolds stress tensor. The most straightforward approach is to associate the unknown Reynolds stresses with the computed mean flow quantities by means of a turbulence model or closure. If the Boussinesq hypothesis is applied, this results in a linear relationship to the mean flow strain tensor through the dynamic eddy viscosity μ_t [1]:

$$\tau_{ij}^R = \mu_t \left(\frac{\partial U_i}{\partial x_j} + \frac{\partial U_j}{\partial x_i} - \frac{2}{3} \frac{\partial U_k}{\partial x_k} \delta_{ij} \right) - \frac{2}{3} \rho k \delta_{ij} \tag{11}$$

where k, also called TKE, is the turbulent kinetic energy and δ_{ij} is the Kronecker delta. We approximate the Reynolds shear stress or cross-correlation $\overline{u'v'}$, by multiplying the so-called kinematic eddy viscosity ν_T and the local velocity gradients, i.e., $\overline{u'v'} = -\nu_T(\partial U_s/\partial n + \partial U_n/\partial s)$, where the overline indicates time-averaged quantity, but it will be omitted in the rest of the paper for simplicity. It was observed that the second velocity gradient values ($\partial U_n/\partial s$) were negligible in all cases, except in the vicinity of the boundary-layer edge at location 3 (APG). The approximated, outer-scaled Reynolds shear stresses are presented in Fig. 21, whereas the inner-scaled stresses are presented in Fig. 22; therefore, either the local edge velocity or the local friction velocity is used for scaling purposes, respectively. The three closure models considered in the present work have a reasonable performance in the ZPG region although overestimating (up to 60%) the stresses compared against the experimental results from Tichenor et al. [4] at $n/\delta \approx 0.2$. On the other hand, the near-wall region is predicted slightly better by two-equation models in locations 1 and 2 (particularly by the SST model) when compared with DNS by Nicholson et al. [7], as a rapid transition to the $k-\omega$ variants superiority is seen inside the boundary layer. All turbulence models significantly overpredict Reynolds shear stresses in the outer portion of the boundary layer at the FPG region. From experiments by [4] and DNS by [7], a remarkable attenuation of $u'v'$ in the convex curvature region (location 2) caused by the FPG is clearly observed. Because peak values of $u'v'$ in location 2 are approximately 1.5 times lower than those of location 1, we may infer that the flow is quasi laminarized or at the verge of relaminarization ("laminarescent" boundary layer) [45]. More information would be needed to infer that, which is beyond the scope of the present paper. Furthermore, the poor performance of RANS turbulence models in capturing the phenomenon of quasi laminarization in initially turbulent boundary layers subject to strong FPG has also been observed in incompressible sink flows [46]. We have seen a decrease in Reynolds shear stresses in the FPG region due to flow acceleration, and an increase of turbulent mixing in the APG region due to the turbulence enhancement, which was also seen in strong APG regions [20] of supersonic turbulent boundary layers.

The inner-scaled stresses in Fig. 22a show a better collapse between all models in the ZPG region. The following DNS data are included: Araya and Jansen [8] at $Re_{\delta 2,\mathrm{comp}} = 4854$, and Duan et al. [36] and Araya et al. [6] at significantly much lower Reynolds numbers; i.e., $Re_{\delta 2,\mathrm{comp}}$ equals to 1578 and 790, respectively, whereas the compressible $Re_{\delta 2}$ in the present RANS was around 3000–3800 according to the selected turbulence model (see Fig. 17b). Furthermore, the Reynolds number dependency in location 1 by contrasting RANS versus DNS can be described as follows: i) there is a clear displacement toward the wall of $u'v'$ peaks as $Re_{\delta 2}$ increases when using outer scaling in the wall-normal direction, and ii) the constant shear layer or "plateau" (region of $u'v'$ peaks) occupies a larger portion in the boundary layer at higher Reynolds numbers. This is consistent to outcomes reported by [47] in supersonic flat plates. Although peak values of $u'v'$ exhibit a moderate reduction in Fig. 22b (location 2) without an obvious plateau, it is important to highlight the meaningful attenuation of $u'v'$ in the inner region. For instance, at a distance from the wall of barely 1% of the boundary-layer thickness (i.e., at $n/\delta \approx 0.01$), the absolute values of $u'v'^+$ intensities are 0.267 at location 1 (ZPG) and 0.0775 at location 2 (FPG). This indicates that the FPG effects are firstly felt in the near-wall region due to the convex curvature given by the presence of a substantial local reduction of $u'v'^+$. Similar observations have been reported by [48] in supersonic turbulent boundary layers with reductions of $u'v'$ of approximately 75% in the near-wall region and a local streamline FPG of −20 kPa/m. Finally, there is an important recovery of the turbulent mixing or $u'v'^+$ in the near-wall region of location 3 (APG). Furthermore, the constant shear layer or plateau has expanded and inclined, ranging nearly $0.02 < n/\delta < 0.2$ in the boundary layer. Each turbulence model has predicted different positive slopes. However, it is important highlighting that RANS predictions were able to capture this enlargement inclination of the constant shear layer caused by APG, as also reported by [49] in incompressible turbulent boundary layers subject to strong streamwise APG via DNS. The observed bump on $u'v'^+$ by the edge of the boundary layer cannot be attributed to some APG induced by the concave curvature. We found out that this was caused by increases of the wall-normal velocity gradient $\partial U_n/\partial s$, as the upstream inviscid flow was accelerated by the convex curvature (see Fig. 11).

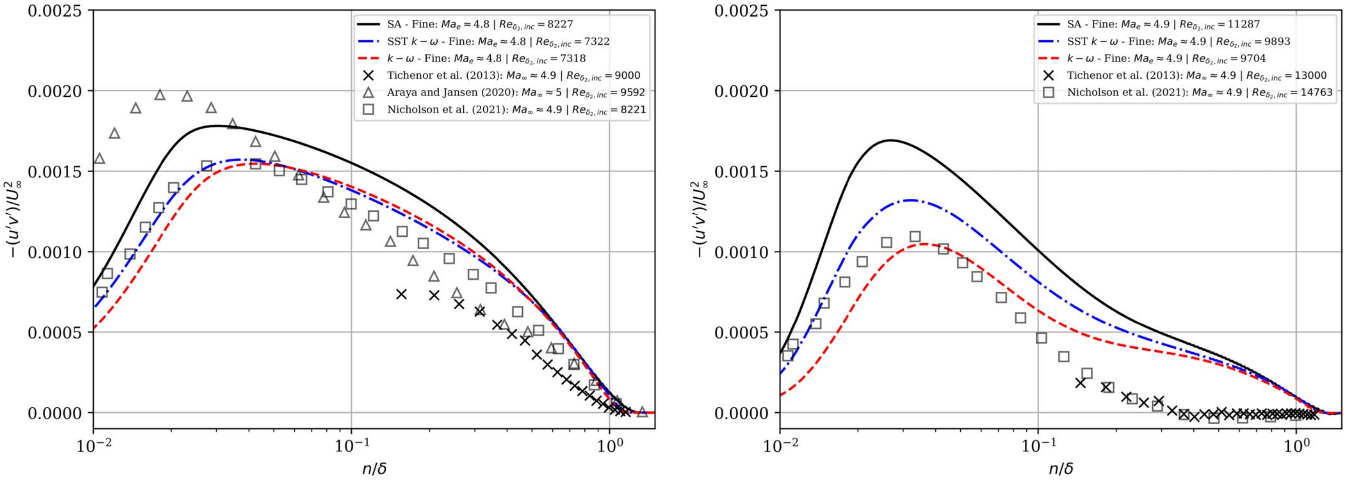

a) Location 1 (ZPG) - outer scaled stresses **b) Location 2 (FPG) - outer scaled stresses**

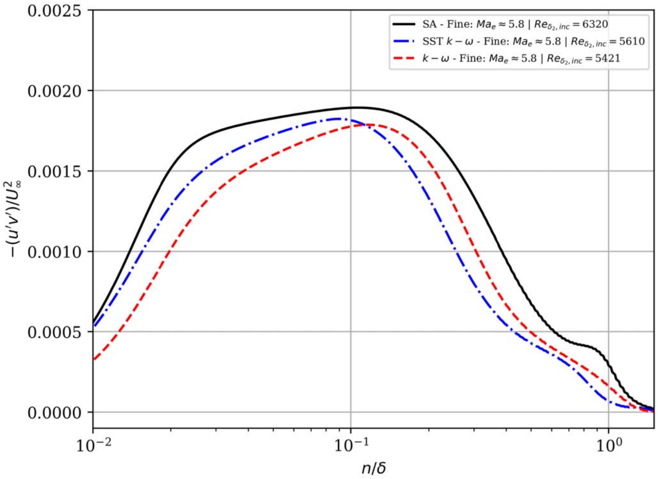

c) Location 3 (APG) - outer scaled stresses

Fig. 21 Reynolds shear stress (outer scaled).

F. Turbulent Kinetic Energy, Specific Dissipation Rate, Production, and Dissipation

The production of TKE in the boundary layer can be assessed by studying one crucial term in the TKE and mean-flow kinetic energy equations, $\mathcal{P}$. According to Pope [50], the mean velocity gradients act against the Reynolds stresses, removing kinetic energy from the mean flow and transferring it to the fluctuating velocity field; hence this term is typically referred to as production of TKE $= 1/23(u'^2 + v'^2 + w'^2)$. The Boussinesq hypothesis leads to a collapse of $\mathcal{P}$ to the rightmost term in Eq. (12).

$$\mathcal{P} \equiv -u_{i'} u_{j'} \frac{\partial U_i}{\partial x_j} \approx \nu_T \left[\frac{\partial U_s}{\partial n} + \frac{\partial U_n}{\partial s} \right]^2 \tag{12}$$

Further, we substitute our approximate relation for the Reynolds shear stress that yields the expression used to model the production of TKE. An increase in this term would suggest a deceleration of the mean flowfield and an enhancement of the fluctuating component of the velocity field. APGs tend to destabilize the boundary layer, experiencing an enhancement of turbulence in the outer portion. Furthermore, the outer streaks are intensified by APG and can be related to local increases of turbulence production and streamwise velocity fluctuations (outer peaks), according to DNS studies by Skote et al. [51] and experimental-numerical invetigation by Vila et al. [52].

For the two-equation models, we can further study more aspects of the TKE and the specific dissipation rate. We have also calculated the TKE production for the SA model due to the nature of the approach. Figure 23a shows TKE profiles for two-equation models (SST and $k-\omega$) at the three streamwise locations and normalized in outer units. Similar performance of SST and $k-\omega$ is observed in the ZPG region with TKE peaks in the buffer region: for the SST model at $n/\delta \approx 0.036$, whereas for the $k-\omega$ model at $n/\delta \approx 0.044$. The peak location roughly remains constant in the FPG region, but peak strengths exhibit an almost 50% decrease. It is worth highlighting the presence of meaningful values of TKE in the outer part of FPG for $n/\delta > 0.2$. A similar TKE profile shape by the $k-\omega$ model has been obtained in DNS of supersonic turbulent boundary layers subject to convex wall curvature [20]. It can be hypothesized that the quasi-laminarization process or TKE attenuation by convex-streamline-curvature-driven flow acceleration begins first in the near-wall region, showing residual values in the outer part of the boundary layer. A similar observation has been discussed in Reynolds shear stress profiles subject to FPG. The most significant differences between SST and $k-\omega$ model in TKE profiles are observed in the outer region of the FPG zone (i.e., for $n/\delta > 0.1$), where SST uses the $k-\varepsilon$ approach. Moreover, for the APG station, the TKE peaks move significantly toward the boundary-layer edge ($n/\delta \approx 0.09$ or $n^+ \approx 50$).

Figure 23b depicts ω profiles. According to Wilcox [1], ω is the dissipation per unit turbulence kinetic energy; thus, the turbulent dissipation rate can be defined as $\varepsilon \sim \omega k$ based on dimensional analysis. Both two-equation models have predicted ω consistently, as expected, because the cross-diffusion term in Eq. (7) induces negligible contribution to the ω-transport equation in the very near-wall region, where maximum specific dissipation occurs. Although the normalized turbulent dissipation at the wall in the FPG region exhibits moderate lower values than those of the ZPG zone (incoming undistorted turbulent boundary layer), the dissipation rate shows a

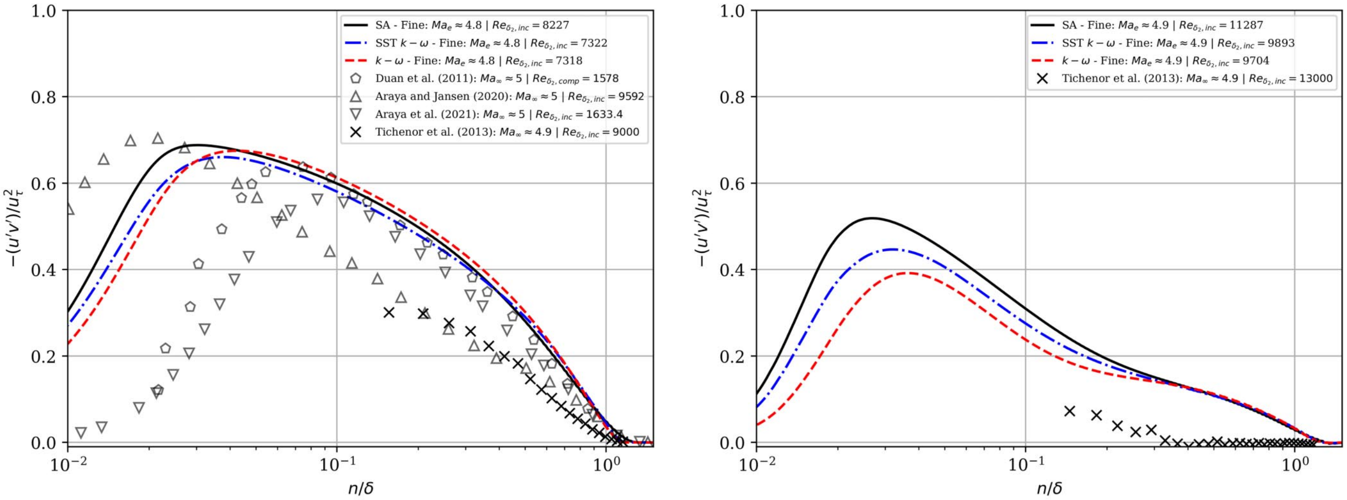

a) Location 1 (ZPG) - inner scaled stresses

b) Location 2 (FPG) - inner scaled stresses

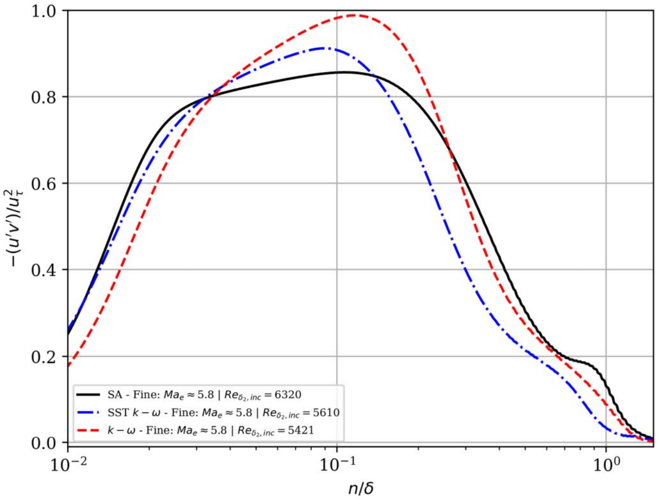

c) Location 3 (APG) - inner scaled stresses

Fig. 22 Reynolds shear stress (inner scaled).

meaningful enhancement by the concave wall curvature or APG region (approx. 65% increase). The dissipation terms of TKE and ω, as in Eqs. (5) and (6), are depicted by Figs. 23c and 23d, respectively. The TKE dissipation term contains explicitly the product $k\omega$, which is proportional to the turbulent dissipation ε. For the three streamwise locations considered (i.e., ZPG, FPG, and APG), maxima of TKE dissipation occur within the boundary-layer zone $0.016 < n/\delta < 0.025$ or $9.5 < n^+ < 11.4$, with largest decreases (about twofold reduction) at the FPG or convex station. This effectively demonstrates a flow tendency toward the quasi-laminarization state. Downstream, the TKE dissipation term at the APG zone exhibits a great recovery by surpassing the incoming ZPG values. Additionally, small humps or inflection points are seen around $0.1 < n/\delta < 0.2$, given by the APG-induced turbulence production. Substantial differences are seen among SST versus $k-\omega$ values for $n/\delta < 0.03$. In Fig. 23d, the dissipation of ω shows up to fourfold increases at the wall of the APG station, with almost identical results by the SST and $k-\omega$ models.

To assess the production of turbulence kinetic energy, we have evaluated the most relevant term in Fig. 23e, as presented in Eq. (12). The outer scaled results follow the expected behavior for ZPG with the location of maximum turbulence production around 1.5–2% of the boundary-layer thickness. Note that this peak in production moves farther from the wall as the Reynolds number decreases (not shown), according to DNS by Araya et al. [6] over an adiabatic hypersonic flat plate. Notice that turbulence production is normalized by outer units (i.e., by local values of δ/U_∞^3). A moderate augmentation in peaks of TKE production due to FPG (except for the $k-\omega$ model) can be seen at location 2, as compared with ZPG peaks. On the other hand, decreases of TKE production peaks were obtained in dimensional units (not shown), indicating a scaling-dependent conclusion. In addition, these maxima are now located roughly $0.015 < n/\delta < 0.02$; thus, wall-normal locations of TKE production peaks are insensible to flow acceleration. Also, peaks of TKE production (at $n^+ \approx 10$–10.5) are decreased due to a concave-streamline-curvature-driven flow deceleration that occurs just before location 3. Secondary outer peaks of turbulence production (as also reported by [49] in strong streamwise APG of incompressible turbulent boundary layers) can be visualized in the region $0.1 < n/\delta < 0.2$, mostly on two-equation models. These outer shoulders (caused by APG, which produces local increases of the term $\partial U_s/\partial n$ as seen in Fig. 16c) on the TKE production profiles are nearly imperceptible. This may be linked to the prescribed moderate concave curvature.

Finally, profiles of ω production are shown by Fig. 23f. As expected, the near-wall region is the largest ω generator. Interestingly, and according to the outer normalization employed, the ω production is maximum at the convex surface, with much larger values by the $k-\omega$ model.

G. Mean Boundary-Layer Quantities

Crocco and Lees proposed two quantities to characterize the mean velocity in the boundary layer and the mean temperature normalized with the edge parameters [18]. We present both quantities in Fig. 24. The thermal boundary layer suffers the most significant distortion as

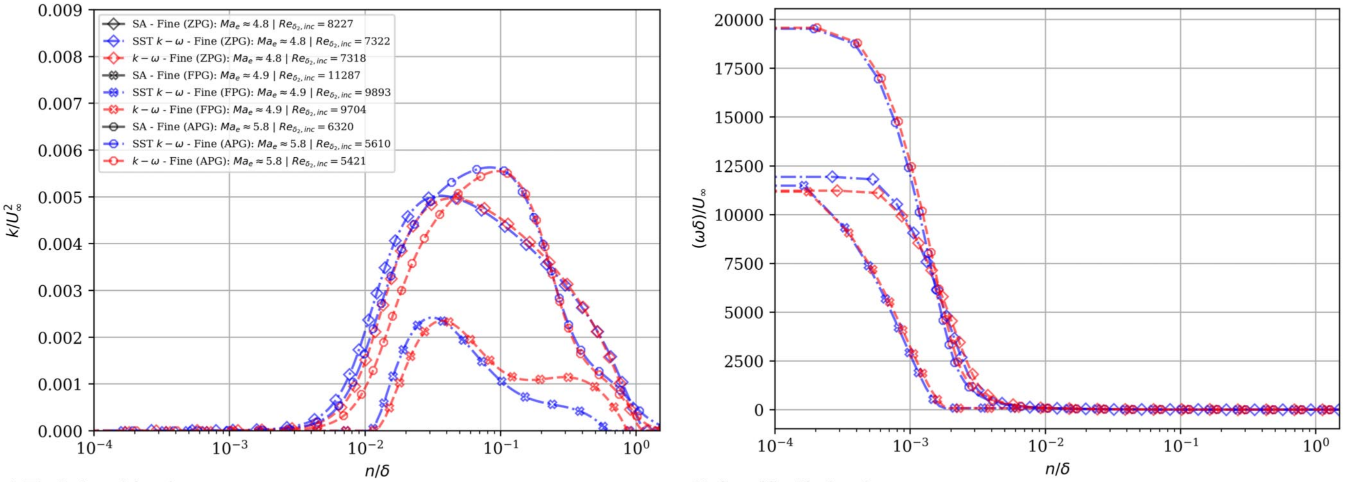

a) Turbulent kinetic energy

b) Specific dissipation rate

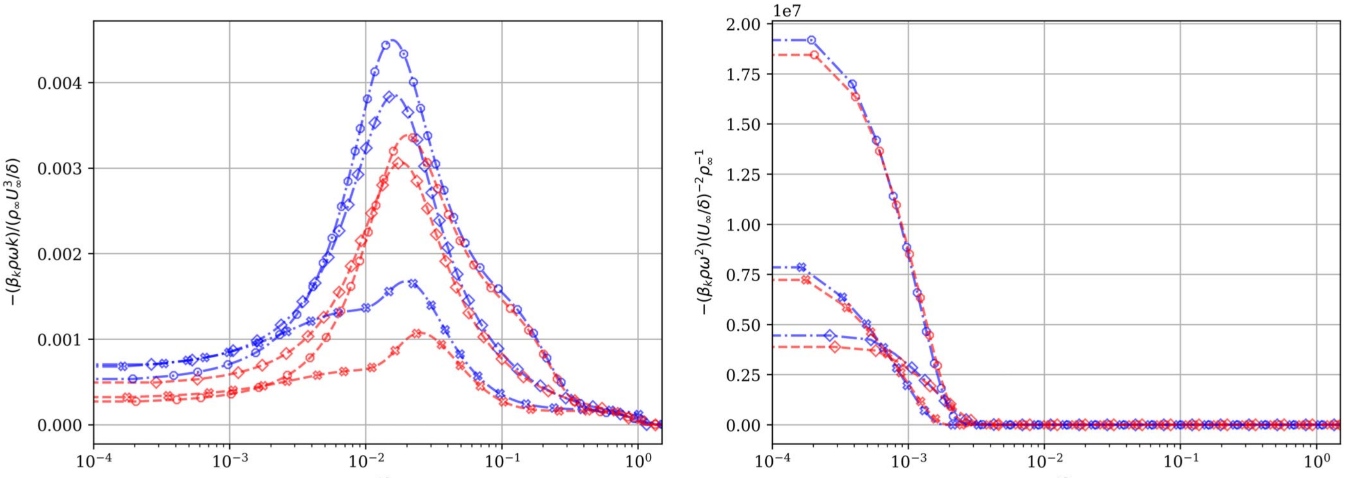

c) TKE Dissipation

d) ω Dissipation

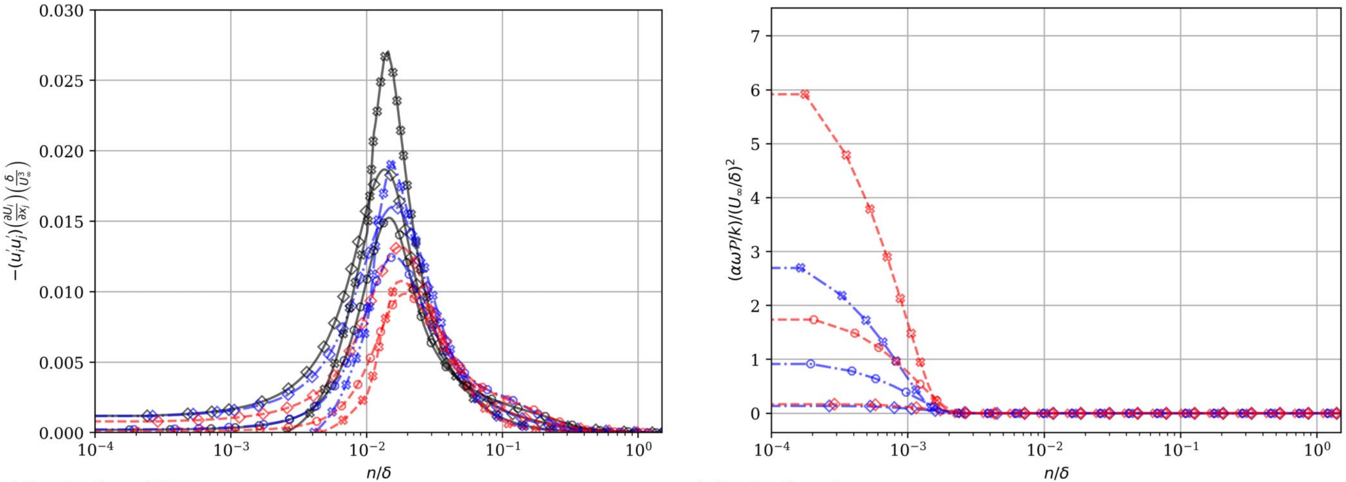

e) Production of TKE

f) Production of ω

Fig. 23 TKE, ω, and their production/dissipation.

seen in Fig. 24b, where a substantial distortion in the boundary-layer temperature is observed in the hypersonic expansion followed by an even greater distortion in the APG region due to the compression. The SA and SST $k-\omega$ models are fairly consistent in their agreement for both the mean boundary-layer velocity and temperature.

H. Strain Rates

Lastly, we also evaluate the performance of the three models in their predictions of strain rates as compared with the experimental data by Tichenor et al. [4] and DNS data by Nicholson et al. [7]. The principal components of the x-y strain rates are $S_{xy} = (\partial U/\partial y + \partial V/\partial x)/2$ and were normalized by local values of δ/U_e. In the ZPG region, up to $n/\delta \approx 0.8$ the SST model generates strain rates very similar to Tichenor's experiments and DNS by [7], whereas the SA model performs better beyond $n/\delta \approx 0.8$ with a smoother transition to the freestream, as seen in Fig. 25a. The in-plane xy strain rates exhibit a mild decrease in the FPG region. This is caused by negative values of $\partial V/\partial x$ in the convex curvature region (with zero value in

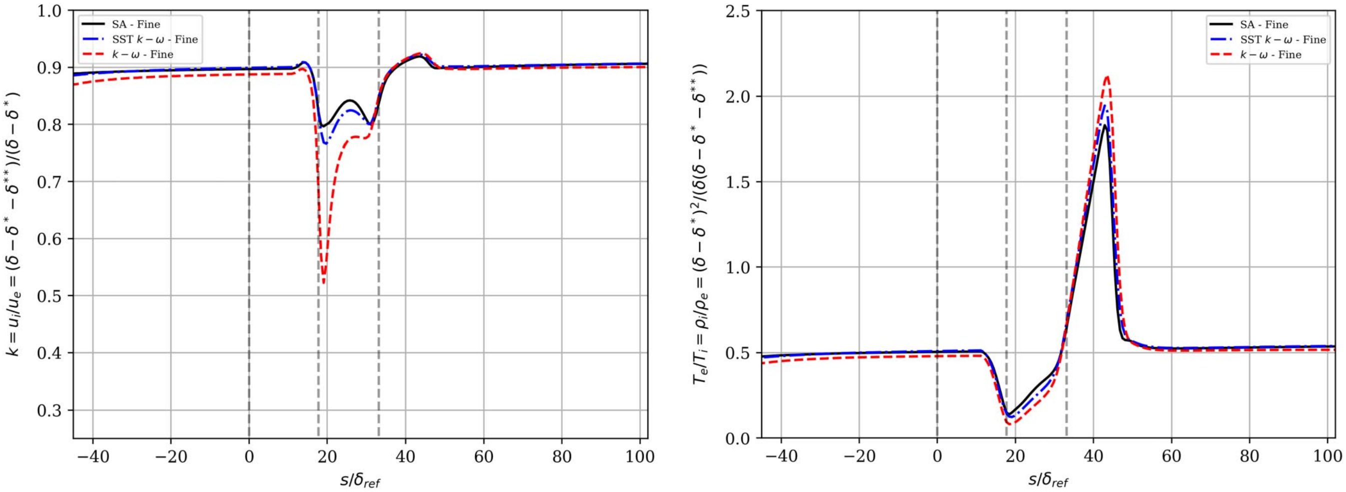

a) Mean boundary layer velocity evolution (with compressibility corrections)

b) Mean boundary layer temperature (with compressibility corrections)

Fig. 24 Mean boundary-layer velocity and temperature as proposed by Crocco and Lees [18]. Vertical dashed lines correspond to locations 1, 2, and 3 (from left to right).

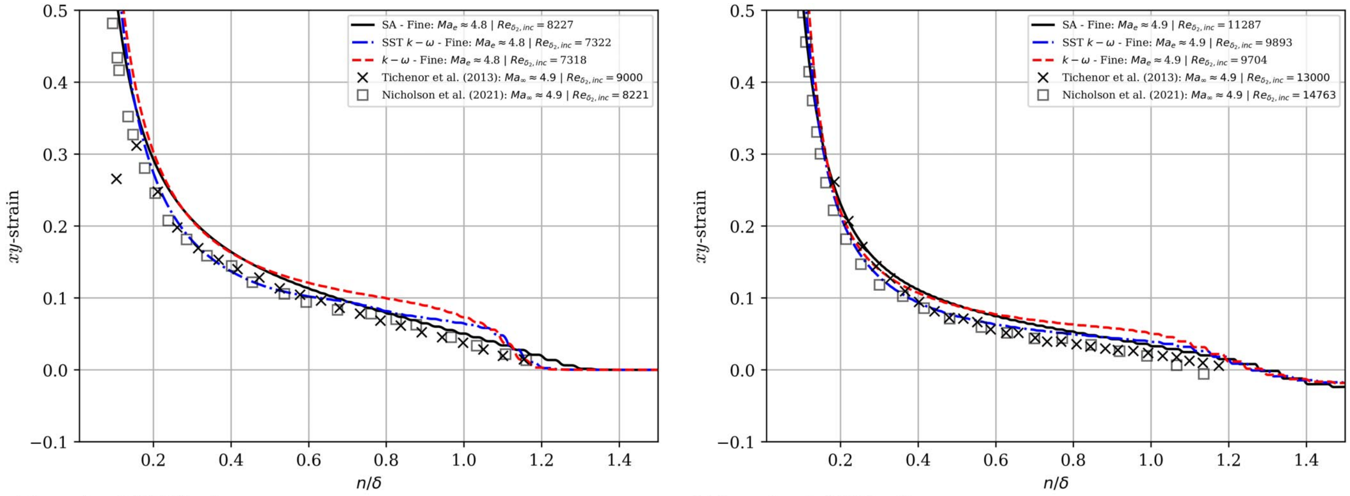

a) Location 1 (ZPG) - S_{xy}

b) Location 2 (FPG) - S_{xy}

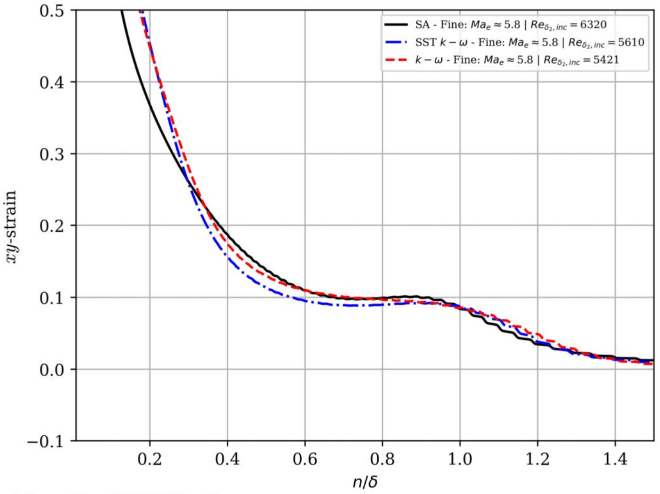

c) Location 3 (APG) - S_{xy}

Fig. 25 In-plane strain rates. Reference points are reproduced from Tichenor et al. [4].

ZPG), as visualized in Fig. 12b. Again, the SST model's strain rates show an excellent agreement with [4,7] up to $n/\delta \approx 0.8$. In the wake region, both SST and SA perform equally, as observed in Fig. 25b.

The APG region in Fig. 25c exhibits a local bulge on S_{xy} toward the boundary layer's edge caused by the upstream flow acceleration due to the convex curvature. In summary, and although all three models tend to exhibit a very similar behavior, the SST $k-\omega$ has a superior performance in the inner portion of the boundary layer. Toward the outer portion and beyond, the SA model exhibits a more physically sound behavior.

IV. Conclusions

In this study, the performance of three widely used turbulence models has been analyzed, namely, the standard $k-\omega$ [1], the SST $k-\omega$ [2], and the SA [3], in curved wall-bounded turbulent flows at the hypersonic regime. The wind-tunnel geometry from Tichenor et al. [4] was replicated; therefore, the following outcomes were drawn based on the previously mentioned configuration. In addition, experiments by [5] and DNS by [6–8] at Mach numbers around 5 have been employed for ZPG and FPG stations. Although the major purpose of the present paper was to evaluate the RANS performance in convex wall curvature-driven FPG flows by direct comparison with experiments by [4], a secondary but still important objective was to elucidate the concave curvature effects. Overall, all turbulence models have demonstrated consistency in predicting first-order flow statistics such as mean velocity, static pressure, and temperature inside the boundary layer and outer freestream values. Different degrees of dispersion were observed in flow parameters at the wall and at the boundary-layer edge (e.g., friction velocity and boundary-layer thickness), more evident in zones of non-ZPG. On the other hand, prediction of the Reynolds shear stresses (or second-order statistics) has been satisfactory in the ZPG zone. Two-equation models were able to capture the tendency of the Reynolds shear stresses in the near-wall region of the convex surface curvature; however, all models have failed to accurately reproduce them in the outer region. Conversely, all models agreed in their thermal/flow boundary-layer relation as studied via their agreement with Walz's equation. The thermal/flow boundary-layer relationship is modeled extremely well by this equation in both the ZPG and FPG regions.

The major terms of the turbulent transport equation budgets for TKE and ω were scrutinized. Whereas peak locations of TKE ($n/\delta \approx 0.036$–0.044) approximately remained unchanged in the FPG region with respect to the ZPG zone, peak strengths showed meaningful decreases (~50%) due to flow acceleration. Furthermore, nonnegligible values of TKE are visualized in the outer part of the boundary layer ($n/\delta > 0.2$) where the most noticeable discrepancies between SST and $k-\omega$ model occur.

Unlike the FPG and ZPG zones, a more notable distortion in the thermal/flow boundary-layer relationship is exhibited in the APG. For instance, wall-normal locations of TKE maxima significantly moved toward the boundary-layer edge ($n/\delta \approx 0.09$). In terms of concave-streamline-curvature-driven effects, all models were able to capture the amplification and inclination (with different quantitative values) of the constant shear layer due to APG influence. Moreover, the outer secondary peaks of TKE production and dissipation due to the APG-induced turbulence production enhancement have been replicated by two-equation models. Some previous DNS studies on decelerating flows have linked these outer peaks on turbulence production to the intensification of large-scale structures by APG [20,49,51,52].

Acknowledgments

Christian J. Lagares-Nieves acknowledges financial support from the Puerto Rico Louis Stokes Alliance for Minority Participation's Bridge to the Doctorate Program from the National Science Foundation under Grant No. HRD-1906130. This material is based upon work supported by the Air Force Office of Scientific Research under award number FA9550-17-1-0051. This work was supported in part by high-performance computer time and resources from the Department of Defense High Performance Computing Modernization Program.

References

[1] Wilcox, D. C., *Turbulence Modeling for CFD*, 3rd ed., DCW Industries, La Cañada, CA, 2006, pp. 107–128, 239–295, 303–334.

[2] Menter, F. R., "Two-Equation Eddy-Viscosity Turbulence Models for Engineering Applications," *AIAA Journal*, Vol. 32, No. 8, 1994, pp. 1598–1605.
https://doi.org/10.2514/3.12149

[3] Spalart, P., and Allmaras, S., "A One-Equation Turbulence Model for Aerodynamic Flows," *30th Aerospace Science Meeting and Exhibit*, AIAA Paper 1992-0439, 1992.

[4] Tichenor, N. R., Humble, R. A., and Bowersox, R. D. W., "Response of a Hypersonic Turbulent Boundary Layer to Favourable Pressure Gradients," *Journal of Fluid Mechanics*, Vol. 722, May 2013, pp. 187–213.
https://doi.org/10.1017/jfm.2013.89

[5] Neeb, D., Saile, D., and Gulhan, A., "Experiments on a Smooth Wall Hypersonic Boundary Layer at Mach 6," *Experiments in Fluids*, Vol. 59, No. 68, 2018, pp. 1–21.
https://doi.org/10.1007/s00348-018-2518-z

[6] Araya, G., Lagares, C., Santiago, J., and Jansen, K., "Wall Temperature Effect on Hypersonic Turbulent Boundary Layers via DNS," *AIAA Scitech 2021 Forum*, AIAA Paper 2021-1745, 2021.
https://doi.org/10.2514/6.2021-1745

[7] Nicholson, G., Huang, J., Duan, L., Choudhari, M. M., and Bowersox, R. D., "Simulation and Modeling of Hypersonic Turbulent Boundary Layers Subject to Favorable Pressure Gradients due to Streamline Curvature," *AIAA Scitech 2021 Forum*, AIAA Paper 2021-1672, 2021.
https://doi.org/10.2514/6.2021-1672

[8] Araya, G., and Jansen, K., "Effects of Wall Curvature on Hypersonic Turbulent Spatially-Developing Boundary Layers," *2020 AFOSR/ONR/HVSI Hypersonic Aerodynamics Portfolios Review*, 2020.
https://doi.org/10.13140/RG.2.2.27763.66081

[9] Candler, G. V., "Rate Effects in Hypersonic Flows," *Annual Review of Fluid Mechanics*, Vol. 51, 2019, pp. 379–402.
https://doi.org/10.1146/annurev-fluid-010518-040258

[10] Park, C., *Nonequilibrium Hypersonic Aerothermodynamics*, Wiley, New York, 1989, pp. 43–80, 119–142, 171–214.

[11] Josyula, E., *Hypersonic Nonequilibrium Flows: Fundamentals and Recent Advances*, AIAA, Reston, VA, 2015, pp. 1–37.
https://doi.org/10.2514/4.103292

[12] Dorrance, W. H., *Viscous Hypersonic Flow: Theory of Reacting and Hypersonic Boundary Layers*, Dover, 2017, pp. 1–8, 173–205.

[13] Leyva, I. A., "The Relentless Pursuit of Hypersonic Flight," *Physics Today*, Vol. 70, No. 11, 2017, p. 30.
https://doi.org/10.1063/PT.3.3762

[14] Bertin, J. J., and Cummings, R. M., "Critical Hypersonic Aerothermodynamic Phenomena," *Annual Review of Fluid Mechanics*, Vol. 38, Jan. 2006, pp. 129–157.
https://doi.org/10.1146/annurev.fluid.38.050304.092041

[15] Huang, J., Bretzke, J.-V., and Duan, L., "Assessment of Turbulence Models in a Hypersonic Cold-Wall Turbulent Boundary Layer," *Fluids*, Vol. 4, No. 1, 2019, p. 37.
https://doi.org/10.3390/fluids4010037

[16] Currao, G. M. D., Choudhury, R., Gai, S. L., Neely, A. J., and Buttsworth, D. R., "Hypersonic Transitional Shock-Wave-Boundary-Layer Interaction on a Flat Plate," *AIAA Journal*, Vol. 58, No. 2, 2020, pp. 814–829.
https://doi.org/10.2514/1.J058718

[17] Paciorri, R., Dieudonné, W., Degrez, G., Charbonnier, J.-M., and Deconinck, H., "Exploring the Validity of the Spalart-Allmaras Turbulence Model for Hypersonic Flows," *Journal of Spacecraft and Rockets*, Vol. 35, No. 2, 1998, pp. 121–126.
https://doi.org/10.2514/2.3307

[18] Crocco, L., and Lees, L., "A Mixing Theory for the Interaction Between Dissipative Flows and Nearly-Isentropic Streams," *Journal of the Aeronautical Sciences*, Vol. 19, No. 10, 1952, pp. 649–676.
https://doi.org/10.2514/8.2426

[19] Kaufman, L. G., Hartofilis, S. A., Evans, W. J., Oman, R. A., Meckler, L. H., and Weiss, D., "A Review of Hypersonic Flow Separation and Control Characteristics," Grumman Aircraft Engineering Corp. TR AD0276714, Bethpage, NY, March 1962, https://apps.dtic.mil/sti/citations/AD0276714.

[20] Lagares, C. J., Jansen, K. E., Patterson, J., and Araya, G., "The Effect of Concave Surface Curvature on Supersonic Turbulent Boundary Layers," *72nd Annual Meeting of the American Physical Society, Division of Fluid Dynamics*, 2019.
https://doi.org/10.13140/RG.2.2.28296.37126

[21] Rivera, E., and Araya, G., "Transport Phenomena in High-Speed Wall-Bounded Flows Subject to Concave Surface Curvature," *Journal of Computational Science Education*, Vol. 12, No. 1, 2021, pp. 16–23.
https://doi.org/10.22369/issn.2153-4136/12/1/3

[22] Menter, F. R., “Review of the Shear-Stress Transport Turbulence Model Experience from an Industrial Perspective,” *International Journal of Computational Fluid Dynamics*, Vol. 23, No. 4, 2009, pp. 305–316. https://doi.org/10.1080/10618560902773387

[23] Donovan, J. F., Spina, E. F., and Smits, A. J., “The Structure of a Supersonic Turbulent Boundary Layer Subjected to Concave Surface Curvature,” *Journal of Fluid Mechanics*, Vol. 259, Jan. 1994, pp. 1–24. https://doi.org/10.1017/S0022112094000017

[24] Funderburk, M. L., and Narayanaswamy, V., “Investigation of Negative Surface Curvature Effects in Axisymmetric Shock/Boundary-Layer Interaction,” *AIAA Journal*, Vol. 57, No. 4, 2019, pp. 1594–1607. https://doi.org/10.2514/1.J057275

[25] López, D., Domínguez, D., and Gonzalo, J., “Impact of Turbulence Modelling on External Supersonic Flow Field Simulations in Rocket Aerodynamics,” *International Journal of Computational Fluid Dynamics*, Vol. 27, Nos. 8–10, 2013, pp. 332–341. https://doi.org/10.1080/10618562.2013.867951

[26] Launder, B. E., Reece, G. J., and Rodi, W., “Progress in the Development of a Reynolds-Stress Turbulence Closure,” *Journal of Fluid Mechanics*, Vol. 68, No. 3, 1975, pp. 537–566. https://doi.org/10.1017/S0022112075001814

[27] “ANSYS Fluent–CFD Software,” ANSYS Fluent, ANSYS, 2020, http://www.ansys.com/products/fluids/ansys-fluent.

[28] van Leer, B., “Towards the Ultimate Conservative Difference Scheme. V. A Second-Order Sequel to Godunov’s Method,” *Journal of Computational Physics*, Vol. 32, No. 1, 1979, pp. 101–136. https://doi.org/10.1016/0021-9991(79)90145-1

[29] Liou, M., and Steffen, C. J., Jr., “A New Flux Splitting Scheme,” *Journal of Computational Physics*, Vol. 107, No. 1, 1993, pp. 23–39. https://doi.org/10.1006/jcph.1993.1122

[30] Liou, M.-S., “A Sequel to AUSM: AUSM+,” *Journal of Computational Physics*, Vol. 129, No. 2, 1996, pp. 364–382. https://doi.org/10.1006/jcph.1996.0256

[31] Huang, T.-H., Wei, H., Chen, J.-S., and Hillman, M. C., “RKPM2D: An Open-Source Implementation of Nodally Integrated Reproducing Kernel Particle Method for Solving Partial Differential Equations,” *Computational Particle Mechanics*, Vol. 7, No. 2, 2020, pp. 393–433. https://doi.org/10.1007/s40571-019-00272-x

[32] Araya, G., “Turbulence Model Assessment in Compressible Flows Around Complex Geometries with Unstructured Grids,” *Fluids*, Vol. 4, No. 2, 2019, p. 81. https://doi.org/10.3390/fluids4020081

[33] Duan, L., and Martín, M. P., “Direct Numerical Simulation of Hypersonic Turbulent Boundary Layers. Part 4. Effect of High Enthalpy,” *Journal of Fluid Mechanics*, Vol. 684, Oct. 2011, pp. 25–59. https://doi.org/10.1017/jfm.2011.252

[34] Versteeg, H. K., and Malalasekera, W., *An Introduction to Computational Fluid Dynamics*, Pearson, Harlow, 2007, pp. 66–97.

[35] Dussauge, J. P., and Gaviglio, J., “The Rapid Expansion of a Supersonic Turbulent Flow: Role of Bulk Dilatation,” *Journal of Fluid Mechanics*, Vol. 174, Jan. 1987, pp. 81–112. https://doi.org/10.1017/S0022112087000053

[36] Duan, L., Beekman, I., and Martín, M. P., “Direct Numerical Simulation of Hypersonic Turbulent Boundary Layers. Part 3. Effect of Mach Number,” *Journal of Fluid Mechanics*, Vol. 672, April 2011, pp. 245–267. https://doi.org/10.1017/S0022112010005902

[37] Osterlund, J., Johansson, A., Nagib, H., and Hites, M., “A Note on the Overlap Region in Turbulent Boundary Layers,” *Physics of Fluids*, Vol. 12, No. 1, 2000, pp. 1–4. https://doi.org/10.1063/1.870250

[38] Fernholz, H., and Finley, P., “A Critical Compilation of Compressible Turbulent Boundary Layer Data,” AGARDograph, AGARD TR ADA045367, Vol. 223, Advisory Group for Aerospace Research and Development, Neuilly-Sur-Seine, France, 1977, https://apps.dtic.mil/sti/citations/ADA045367.

[39] Stolz, S., and Adams, N., “Large-Eddy Simulation of High-Reynolds-Number Supersonic Boundary Layers Using the Approximate Deconvolution Model and a Rescaling and Recycling Technique,” *Physics of Fluids*, Vol. 15, No. 8, 2003, pp. 2398–2412. https://doi.org/10.1063/1.1588637

[40] Guarini, S., Moser, R., Shariff, K., and Wray, A., “Direct Numerical Simulation of a Supersonic Turbulent Boundary Layer at Mach 2.5,” *Journal of Fluid Mechanics*, Vol. 414, No. 1, 2000, pp. 1–33. https://doi.org/10.1017/S0022112000008466

[41] Simpson, R., “Turbulent Boundary Layer Separation,” *Annual Review of Fluid Mechanics*, Vol. 21, No. 1, 1989, pp. 205–232. https://doi.org/10.1146/annurev.fl.21.010189.001225

[42] Clauser, F. H., *The Turbulent Boundary Layer*, Elsevier, Amsterdam, The Netherlands, 1956, pp. 1–51. https://doi.org/10.1016/S0065-2156(08)70370-3

[43] Walz, A., and Oser, H., *Boundary Layers of Flow and Temperature*, M.I.T. Press, 1969, https://books.google.com.pr/books?id=ZPJQAAAAMAAJ.

[44] Zhang, Y.-S., Bi, W.-T., Hussain, F., and She, Z.-S., “A Generalized Reynolds Analogy for Compressible Wall-Bounded Turbulent Flows,” *Journal of Fluid Mechanics*, Vol. 739, Jan. 2014, pp. 392–420. https://doi.org/10.1017/jfm.2013.620

[45] Narasimha, K., and Sreenivasan, K. R., “Relaminarization of Fluid Flows,” *Advances in Applied Mechanics*, Vol. 19, Elsevier, New York, 1979, pp. 221–309. https://doi.org/10.1016/S0065-2156(08)70311-9

[46] Saltar, G., and Araya, G., “Reynolds Shear Stress Modeling in Turbulent Boundary Layers Subject to Very Strong Favorable Pressure Gradient,” *Computers & Fluids*, Vol. 202, April 2020, Paper 104494. https://doi.org/10.1016/j.compfluid.2020.104494

[47] Araya, G., Lagares, C., and Jansen, K., “Reynolds Number Dependency in Supersonic Spatially-Developing Turbulent Boundary Layers,” *2020 AIAA SciTech Forum*, AIAA Paper 2020-0574, 2020. https://doi.org/10.2514/6.2020-0574

[48] Luker, J. J., Bowersox, R. D. W., and Buter, T. A., “Influence of Curvature-Driven Favorable Pressure Gradient on Supersonic Turbulent Boundary Layer,” *AIAA Journal*, Vol. 38, No. 8, 2000, pp. 1351–1359. https://doi.org/10.2514/2.1134

[49] Araya, G., and Castillo, L., “Direct Numerical Simulations of Turbulent Thermal Boundary Layers Subjected to Adverse Streamwise Pressure Gradients,” *Physics of Fluids*, Vol. 25, No. 9, 2013, Paper 095107. https://doi.org/10.1063/1.4820816

[50] Pope, S. B., *Turbulent Flows*, Cambridge Univ. Press, 2000.

[51] Skote, M., Henningson, D. S., and Henkes, R. A. W. M., “Direct Numerical Simulation of Self-Similar Turbulent Boundary Layers in Adverse Pressure Gradients,” *Flow, Turbulence and Combustion*, Vol. 60, No. 1, 1998, pp. 47–85. https://doi.org/10.1023/A:1009934906108

[52] Vila, C. S., Orlu, R., Vinuesa, R., Schlatter, P., Ianiro, A., and Discetti, S., “Adverse-Pressure-Gradient Effects on Turbulent Boundary Layers: Statistics and Flow-Field Organization,” *Flow, Turbulence and Combustion*, Vol. 99, No. 3, 2017, pp. 589–612. https://doi.org/10.1007/s10494-017-9869-z

J. Larsson
Associate Editor